ARTICLE

A Composite Surface Configuration towards Improving Cycling Stability of Li-Rich Layered Oxide Materials

Received 00th January 20xx,
Accepted 00th January 20xx

DOI: 10.1039/x0xx00000x

Zhepu Shi,[a, b] Qingwen Gu,[a] Liang Yun,[a] Zhining Wei,[a, c] Di Hu,[b] Bao Qiu,*[a] George Zheng Chen,*[d] and Zhaoping Liu*[a]

Li-rich layered oxides are promising positive electrode candidates for next-generation high energy Li-ion batteries. However, they suffer from a severe gas release issue and side reaction induced surface degradation resulting in a significant capacity fade and voltage decay. Herein, this work proposes a composite surface configuration through coordinating three different structures from Nb/Al surface doping, surface oxygen vacancies and Al_2O_3 layer *via* solution coating. Comprehensive characterizations provide persuasive evidence that the composite surface configuration not only mitigates oxygen release, but also regulates Li^+ ions extraction/insertion during cycling. Due to the reduced side reaction and promoted surface stability, a decent specific discharge capacity of about 270 mAh g^{-1} at 0.1 C between 2.0 and 4.6 V *vs.* Li^+/Li is achieved with 57.0% capacity preservation after 1000 cycles at 1 C. Most importantly, a 20-Ah pouch cell fabricated with this surface-modified positive electrode and a SGC/Gr negative electrode delivers 345 Wh kg^{-1} in specific energy and retains its 77.9% at 0.2 C after 340 cycles.

Introduction

The prosperous market of electric vehicles expedites the development of Li-ion batteries (LIBs) and vice versa. Accompanied by the exposure of the endurance and power limits of electric vehicles, a pressing demand on LIBs with high specific energy and promising lifespan is emerged to break through the present dilemma for electric vehicles. As a reliable positive electrode material with available capacity over 250 mAh g^{-1}, Li-rich layered oxides (hereafter abbreviated as LR-NCM), formularized as $xLi_2MnO_3{\cdot}(1\text{-}x)LiTMO_2$ (TM=Ni, Co, Mn), are appreciated for dealing with the issue of specific energy by researchers.[1, 2] However, the main utilization of these materials is still restricted owing to several drawbacks,[3, 4] such as low initial Coulombic efficiency, limited rate capability and poor cycling stability. In general, these issues are originated from the oxygen redox process at high potential (over 4.5 V *vs.* Li^+/Li).[5] The triggered surface oxygen ions with weak metal-oxygen bond are released as O_2 and left oxygen vacancies on surface.[6] As known as gas release, it is a potential time bomb to cause catastrophic failures of batteries owing to the highly reactive O_2 with flammable electrolytes.[7] Moreover, oxygen release during cycling is likely to bring about the side reactions between positive electrodes and electrolytes, leading to a rise of CO_2 release aside from the decomposition of carbonate electrolytes.[8, 9] Overall, the safety and stability of batteries fabricated from LR-NCM positive electrode materials are both under the threaten from oxygen release. Thus, the ability of reducing oxygen release is a crucial indicator to evaluate the feasibility of LR-NCM positive electrode for practical and large-scale utilization.

Since O_2 are initiated from the instable surface, numerous surface modifications including coating[10, 11], surface doping,[12] surface structure/element control,[13-15] and their combinations,[16, 17] have been proposed to effectively mitigate irreversible O_2 release. For instance, some surface doping methods replace weak TM-O with strong Nb-O bonding,[12, 18, 19] The passivated surface oxygen ions are restricted from breaking related bonds and further dimerization.[20] While other surface ions, such as Al^{3+} ions, show applausive effects on preventing surface degradation.[21] Moreover, Al_2O_3 protective layers are proved to maintain surface integrity once resist the corrosion from the electrolytes.[17] However, rooted in the inseparable oxygen redox, those doped and coated LR-NCM positive electrolytes often sacrifice their capacity as a cost to eliminate oxygen release.[22] Alternately, oxygen vacancies outperform aforementioned methods by endowing high discharge capacity with suppressed oxygen release.[13] The formed oxygen vacancies reduce the migration barrier of lithium ions and trigger O^{2-}/O^- redox couple in the bulk. Noted that lacking precise control is liable to expose LR-NCM positive electrodes to detrimental side reactions and TM dissolution with excessive oxygen deficient layer.[23] To this end, an exclusive modification often fails to fulfill the expectation that settling the critical

[a] *Ningbo Institute of Materials Technology and Engineering, Chinese Academy of Sciences (CAS), Ningbo, 315201, China*
[b] *Department of Chemical and Environmental Engineering, Faculty of Science and Engineering, The University of Nottingham, Ningbo, 315100, China.*
[c] *School of Chemical Engineering and Technology, China University of Mining and Technology (CUMT), Xuzhou, 221166, China.*
[d] *Department of Chemical and Environmental Engineering, Faculty of Engineering, The University of Nottingham, Nottingham, NG7 2RD, United Kingdom*
†Electronic Supplementary Information (ESI) available: [details of any supplementary information available should be included here]. See DOI: 10.1039/x0xx00000x

oxygen release issue with appealing capacity and stability. Therefore, a subtle design in surface structure is essential for obtaining superior electrochemical performance LR-NCM positive electrodes with guaranteed restraint on surface oxygen.

In this work, we propose a composite surface configuration that consists of doped Nb and Al, surface oxygen vacancies and discontinuous Al_2O_3 protective layer on the surface of LR-NCM as shown in **Scheme 1**. Aberration-corrected high-angle annular-dark-field scanning transmission electron microscopy (HAADF-STEM), electron energy loss spectroscopy (EELS), Raman and X-ray photoelectron spectroscopy (XPS) reveal the existence of oxygen vacancies assisted spinel-like phases with corporation of Nb^{5+} and Al^{3+} ions. Differential electrochemical mass spectrometry (DEMS) and gas chromatography (GC) demonstrate the reduced oxygen release with reserved anionic capacity. Transmission electron microscope (TEM) analysis exhibits a unique structure evolution of the composite surface after gas evolution. Galvanostatic intermittent titration technique (GITT) measurement unravels the synergistic contribution of this composite configuration on regulating the Li^+ ions diffusion. A reduced diffusivity of Li^+ ions during oxygen redox verifies the good restraint on surface oxygen and the limited phase transformation. In addition, comprehensive characterization from XPS and Ar^+ etching on O 1s spectra indicate a well-maintained surface attributed to controlled side reactions. As a result, the modified LR-NCM (M-LR-NCM) shows excellent stability over 1000 cycles with negligible capacity decay per cycle (0.091 mAh g^{-1}). Furthermore, full pouch cells with specific energy of 345 Wh kg^{-1} are successfully fabricated with the superior electrochemical performance during cycling at 2.0-4.5V to illustrate the effectiveness of this composite configuration strategy.

Experimental methods

Materials preparation

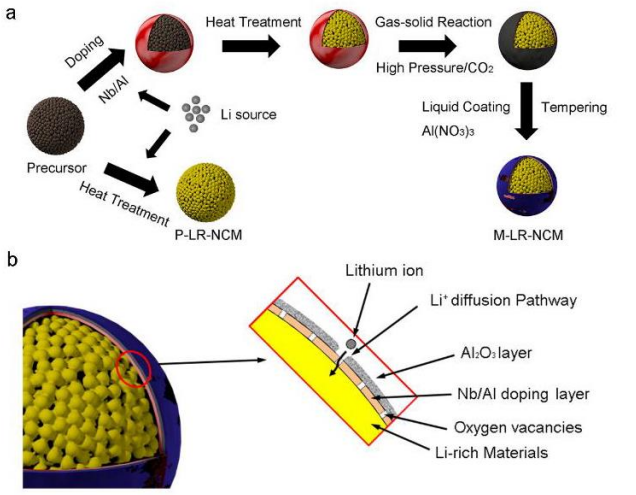

Scheme 1. (a) A schematic illustration of the materials preparation procedures for pristine LR-NCM (P-LR-NCM) and modified LR-NCM (M-LR-NCM). (b) Diagram of proposed model of LR-NCM with a composite surface modification.

The LR-NCM with a formula of $Li_{1.143}Mn_{0.544}Co_{0.136}Ni_{0.136}O_2$ was synthesized by solid-state reactions between spherical $(Mn_{4/6}Ni_{1/6}Co_{1/6})CO_3$ precursor and Li_2CO_3. The same experiment procedures were also reported in our previous papers.[13, 17] The precursors were prepared through a coprecipitation method with a desired stoichiometric ratio of $NiSO_4{\cdot}6H_2O$, $CoSO_4{\cdot}7H_2O$, $MnSO_4{\cdot}4H_2O$ and Na_2CO_3 aqueous solution. Then the obtained spherical $(Mn_{4/6}Ni_{1/6}Co_{1/6})CO_3$ precursors were mixed with proper amounts of Li_2CO_3. The mechanically mixed powders were heated in air at 500 ˚C for 5 h followed by calcinating at 850 ˚C for 16 h. Then, they were cooled to room temperature at furnace. The as-obtained sample was labelled as P-LR-NCM. The composite surface modification process was carried out as follows: a set amount of spherical $(Mn_{4/6}Ni_{1/6}Co_{1/6})CO_3$ precursors and a given trace amount of niobium oxides and aluminium oxides were mixed together with proper amounts of Li_2CO_3. Then the mixture was subjected to the same heat treatment as P-LR-NCM. Next, the sintered materials were placed in an enclosed reactor with desired high pressure via pumping adequate CO_2. With the temperature at 200 ˚C, the gas solid reaction started to form Li_2CO_3 which could be removed after coating/washing and further left oxygen vacancies on the surface. Once the gas-solid reaction finished after 10 h, the treated materials were directly added into $Al(NO_3)_3$ solutions with specific molarity and dispersed under vigorous stirring for 30 min at a fixed pH value of 7. Right after that, filtration process was employed. Afterwards, abundant deionized water was used to wash and filtered materials to remove the residual on the surface. Finally, after washing several times, the washed intermediates covered with oxygen vacancies and Al_2O_3 nucleus were tempered at a low temperature of 500 ˚C for 6 h in air, then cooled down naturally in the furnace to obtain final products, the obtained sample was denoted as M-LR-NCM.

Materials characterization

The crystal structure of the materials was measured by XRD (D8 Advance, Bruker AXS) using Cu-kα radiation. Rietveld refinements of XRD patterns were carried out via FullProf software based on single phase model. Micro-strain values were estimated via JADE software. Chemical analyses of element amounts were measured by ICP-OES (Optima 2100, Perkin-Elmer). Morphology observations were carried out by Field emission scanning-electron microscope (Hitachi S-4800). HAADF-STEM images were recorded using a field scanning transmission electron microscope equipped with image and probe aberration corrector (Spectra 300, ThermoFisher) to detect the atomic morphology of the modified electrode. EELS spectra and EDS mapping were carried out by using Tecnai F20 transmission electron microscope. Talos F200x transmission electron microscope was employed to collected related HRTEM images of modified electrode before and after cycling. The surface structure was analyzed through a Raman spectrometer (Renishaw in Via Reflex) coupled with a 532 nm excitation laser source. Cross-section specimens were prepared and analysed by using focused ion beam microscopy with EDX (Helios G4 CX, Thermo scientific). XPS measurements were carried out with an

X-ray photoelectron spectrometer (Kratos AXIS Ultra DLD) with Al Kα radiation (1486.6 eV). Depth profiling was performed by Ar ion-beam sputtering at ~ 8 keV, and data was collected every 1 min for 5 min in total. Calibration of the peak position of surface elements was based on the graphitic peak in the C 1s spectra at 284.6 eV. Cycled specimens for XPS and Raman were derived from disassembled electrodes after cycling. XRD specimens were powder derived from dried electrodes in argon-filled glove box (H_2O<0.1 ppm O_2< 0.1 ppm) after immersing in dimethyl carbonate. Thermal analyses were conducted by a Differential Scanning Calorimeter (Pyris Diamond DSC, PerkinElmer), via sealing the charged materials in a stainless steel crucible at a pure nitrogen atmosphere with contacting to a trace amount of electrolyte. The heating rate was 10 °C/min. The specific surface energy was measured through BET test (ASAP2020HD88, Micromeritics). The verification of oxygen with unpaired electron was conducted through electron paramagnetic resonance (E500, Bruker). The frequency of electromagnetic wave was 9.842799E09.

Electrochemical measurements

CR2032-type coin cells were used for the electrochemical tests in this work. The half-cells were fabricated with lithium metal negative electrode, LR-NCM positive electrode, 1 M $LiPF_6$ in the ethylene carbonate and diethyl methyl carbonate (EC: DMC 3:7, v/v) with 2 wt.% fluoroethylene carbonate (Zhangjiagang Guotai-Huarong New Chemical Materials Co., Ltd.) as electrolyte (to mitigate high voltage decomposition of electrolyte), and Celgard 2502 polypropylene separator. The positive electrodes were prepared by casting the slurry with a mixture of P-LR-NCM or M-LR-NCM (80 wt.%), Super-P (SP) (10 wt.%), and poly (vinylidene fluoride) binder (PVDF) (10 wt.%) on an aluminium foil. Electrode discs of 13-mm were punched from the positive electrode and pressed at 4 MPa per disc after drying at 80 °C to remove the solvent. After drying at 120 ˚C in a vacuum oven for 4 h. The coin cells were assembled in a full of argon gas glovebox. The mass loading of positive electrode was about 6 mg cm^{-2}. The galvanostatic charge and discharge tests were under a constant current between 2.0 and 4.6 V *vs.* Li^+/Li through a LAND-CT2001A battery tester (Wuhan, China) at room temperature (25 ˚C). The specific current of 250 mA g^{-1} is equal to 1 C rate. The CV and the GITT was carried out by using an electrochemical workstation (Solatron, 1470E) using CR2032-type coin cells. GITT was performed with constant current (10 mA g^{-1}) for 30 min followed by 240 min relaxation with an upper voltage of 4.6 V and a lower limit of 2.0 V. For calculating chemical diffusion coefficient of Li, a simplified method and the formula was listed below:[24]

$$D_{Li^+} = \frac{4}{\pi\tau}\left(\frac{mV_M}{M\,S}\right)^2\left(\frac{\Delta E_S}{\Delta E_t}\right)^2 \quad (1)$$

Operando DEMS measurements

Operando DEMS analysis was carried out to detect the gases generated during the initial charge-discharge process. The DEMS cell was assembled into Swagelok-type cells, using metallic Li as the counter in an Ar-filled glove box. In all, 1 M $LiPF_6$ in 3:7 (volume ratio) mixture of ethylene carbonate-dimethyl carbonate (Zhangjiagang Guotai-Huarong New Chemical Materials Co., Ltd.), and a glass-fiber filter (Whatman GF/D) was used as separator. Electrodes were prepared by casting a slurry with a composition of 80 wt.% active materials (P-LR-NCM or M-LR-NCM), 10 wt.% SP and 10 wt.% PVDF on to an aluminium foil. Subsequently, the electrode discs of 13-mm were punched from the positive electrode and pressed at 4 MPa per disc after drying at 80 ˚C to remove the solvent. The mass loading of positive electrode was about 12 mg cm^{-2}. Then, the electrode was dried at 120 ˚C in a vacuum oven for 4 h. Next, the cell was connected to the mass spectrometer (Linglu Instrument (Shanghai) Co., Ltd) and the electrochemical workstation (Solatron, 1470E). The cell was charged to 4.8V and then discharged to 2.0V for one cycle through electrochemical workstation at 0.1 C. The cell was purged continuously with He gas, which flowed from the cell into the mass spectrometer carrying the evolved gases for MS analysis. The mass signals were recorded as a function of time and the cell voltage. In accordance with the previous studies,[13] only O_2 and CO_2 were evolved during the initial cycle. Furthermore, the detected CO_2 (m/z=44) and O_2 (m/z=32) were normalized on the basis of the ionic currents in the mass spectrometry data with the ionic current of carrying gas He (m/z=4) and the relative mass of active materials.

GC measurement

GC measurement was carried to quantify the respective contribution of CO_2 and O_2 to the integrated gas release. To enlarge the quantity of gas release, 1 Ah scale home-made pouch cells were fabricated to harvest gas. The positive electrodes consist of P-LR-NCM (or M-LR-NCM), SP, single-walled carbon nanotubes (SWCNTs), carbon nanotubes (CNT) and PVDF mixed in NMP with a weight ratio of 95:2.5:0:0:2.5 (P-LR-NCM) and 97.35:0.55:0.1:0.5:1.5 (M-LR-NCM), while the negative electrodes were pure metallic Li. After injecting electrolyte, pouch cells were assembled and stored at room temperature for at least two days. Subsequently, the pouch cells were evacuated and reassembled simultaneously to remove residual gas. The cells were charged to 4.8V and then discharged to 2.0V for one cycle. Next, the cycled pouch cells were transferred in an Ar-filled glove box. A gas-tight syringe was used to transfer 10 μL of the resultant gas from pouch cells into a well-sealed empty gas pocket used for GC system (Agilent, 7890) in the glove box. After transferring the gas pocket out of the glove box, the gas pocket was gradually pressed for 2 min to inject adequate resultant gas into GC. To eliminate the effects from Ar atmosphere during collecting, Ar was used as the carrier gas. To make the result reliable, parallel tests were employed for P-LR-NCM and M-LR-NCM. And all the results are normalized on the basic of the relative mass of active materials.

Full cells measurements

In the full-cell configuration, the negative electrodes consist of 95.5 wt.% SGC/Gr (48 wt.% SGC and 47.5 wt.% graphite, the details of SGC were reported in our previous paper),[25] 2 wt.% styrene butadiene rubber (SBR), 0.1 wt.% SWCNTs, 0.9 wt.% SP,

and 1.5 wt.% aqueous binder (CMC). The relevant half-cell performance is exhibited in **Figure S1**. 20 Ah pouch cells were assembled in a clean room. The positive electrodes consist of M-LR-NCM, SP, SWCNTs, CNT and PVDF mixed in NMP with a weight ratio of 97.35:0.55:0.1:0.5:1.5. Prior to assembling, negative electrodes were pressed with ultrathin Li-foil to complete the pre-lithiation process. Then, the electrochemical evaluation was performed in LAND-CT2001A battery tester at room temperature (25 ˚C). The full cells were first cycled at 0.1C between 2.0 to 4.6 V by performing CC-CV type cycling for one cycle to fully activate the positive electrodes. Then they were cycled between 2.0 to 4.5 V for subsequent cycling at 0.2C. The N/P ratio, defined by total capacity ratio between negative electrodes and positive electrodes, was chosen to be 1.03.

Results and discussion

Pre-cycling materials investigation

The X-ray diffraction (XRD) characterization and corresponding Rietveld refinement were used to reveal the structural details of as-prepared P-LR-NCM and M-LR-NCM. As shown in **Figure 1**a and b, similar long-range orderings are emerged in both samples. All strong peaks are indexed to R-3m space group of α-$NaFeO_2$ crystal domain, while the weak ones between 20° and 23° are ascribed to distinguished $LiMn_6$ superlattice orderings in C/2m space group of monoclinic Li_2MnO_3.[22, 26] The clear splits of (006)/(102), (018)/(110) indicate the layered features of both samples.[27] Specifically, the calculated lattice parameters are slight increased from a = 2.8503 Å and c = 14.240 Å for P-LR-NCM to a = 2.8514 Å and c = 14.241 Å for M-LR-NCM, which are attributed to the trace doped larger ionic radius of Nb^{5+} (0.64 Å).[19] The c/a ratio are 4.9960 and 4.9944 for P-LR-NCM and M-LR-NCM, respectively. The reduced value of c/a for M-LR-NCM illustrates a slight growth of local defects among prominent layered structures.[28, 29] In this case, without increased microstrain (**Table S1**), the defects for M-LR-NCM tends to be the spinel-like/rocksalt phase originated at the surface due to the presence of oxygen vacancies, which is verified in subsequent transmission electron microscope (TEM) characterization.[13] The results based on the inductively coupled plasma optical emission spectrometry (ICP-OES) are listed in **Table S2** to reveal the evolution of chemical composition. The changed molar ratio of metal elements for M-LR-NCM suggests that introducing composite surface structure is accompanied with the slight loss of cations. In accordance with the previous papers,[16, 30] the more loss of nickel and cobalt than manganese elucidates a transformed surface due to the preference of nickel and cobalt on segregating on the surface.[31] Overall, this method has capability to induce the variation on the surface without altering the bulk structure.

The morphologic evolution caused by introducing composite surface was investigated via scanning electron microscopy (SEM) and TEM. As shown in **Figure 1**c and d, both samples represent secondary spheres consisting of abundant primary particles with sizes of about 100 nm. Along with the CO_2 bubbling during the decomposition of carbonate precursors at high temperature, prevailing tiny channels spread between the primary nanoparticles for P-LR-NCM.[19] In comparison with P-LR-NCM, M-LR-NCM has a smooth and discontinuous surface layer with low-conductivity materials, which is ascribed to the introduction of Al_2O_3 layer. The distributed layer with hardly detected pores does not reduce the specific surface area but rather enlarges it. The surface area of M-LR-NCM is 6.0246 m^2 g^{-1}, while the surface area of P-LR-NCM is 4.6364 m^2 g^{-1}. The fundamental lies in a fact that well-distributed spinel-like phases exhibited from **Figure 1**e provide extra 3D diffusion channels on the surface.[13, 16] An enlarged high-angle annular-dark-field (HAADF) image unambiguously shows the distinct atomic arrangements of heavy ions for the surface and the bulk. The local structures with Fd-3m space group spread in the surface of M-LR-NCM about five to six atomic layers, while the rest structures are R-3m space group. In accordance with the Raman results (**Figure S2**), the finite spinel-like phases cause a slight rise at 660 cm^{-1} for M-LR-NCM, which reflects a special stretching mode of shorter M-O bond in spinel-like/rocksalt structures as compared to typical M-O bond at 600 cm^{-1} in layer structures.[17, 30, 32] Additionally, since defects play a role on phonons in Raman characterization,[29] the significant deviation of spinel phase implies a doped surface layer accompanied with oxygen vacancies. Line scan results from electron energy loss spectroscopy (EELS) (**Figure 1**g and **Figure S3**) persuasively prove the existence of doped ions and oxygen vacancies at the surface with characteristic peaks of Al $L_{2,3}$, Nb $M_{4,5}$ and reduced O pre-peak intensities.

To unravel the relative elemental composition of surface layer, energy-dispersive X-ray spectroscope (EDX) was carried on the cross-section of M-LR-NCM sample. As shown in **Figure S4**a, the diameter of the spheres is about 16 µm. A detailed distribution of Nb and Al along with the EDX line scan influenced by interdiffusion is given in **Figure S4**b.[33] Besides, it is noted that the concentration of Nb and Al is relatively small as compared to other elements (Ni, Co, Mn and O) (**Figure S5**), verifying that our method successfully confined introduced elements (Nb and Al) at the surface region with trace quantity. The energy dispersive spectroscopy (EDS) mapping from TEM provide consistent results as shown in **Figure S6**. Moreover, the gradient involved surface forms an interlayer region, which guarantees the Li^+ conductivity,[17] and promotes Li^+ ion migration through Li layer.[19]

X-ray photoelectron spectroscopy (XPS) measurements were made to investigate the different chemical structure of M-LR-NCM after the surface modification. As shown in **Figure 1**h-j, the calibrated spectra of Co 2p, Mn 2p and Ni 2p for P-LR-NCM and M-LR-NCM exhibit negligible changes for the peak shape. Coinciding with the previous references,[17, 34] the dominant peaks of $2p_{3/2}$ at binding energies of about 642, 780 and 855 eV indicate the Mn^{4+}, Co^{3+} and Ni^{2+} in P-LR-NCM and M-LR-NCM, respectively. It is worth mentioning that, a slight shift towards high binding energies for M-LR-NCM can also be detected, demonstrating the chemical valences of the TM ions are elevated after treated surface. As shown in **Figure 1**k and l, the clear Al 2p signals appear at 73.7 eV,[17] while the Nb $3d_{3/2}$ and Nb $3d_{5/2}$ peaks emerge at 210.1 eV and 207.4 eV,[35] both validate

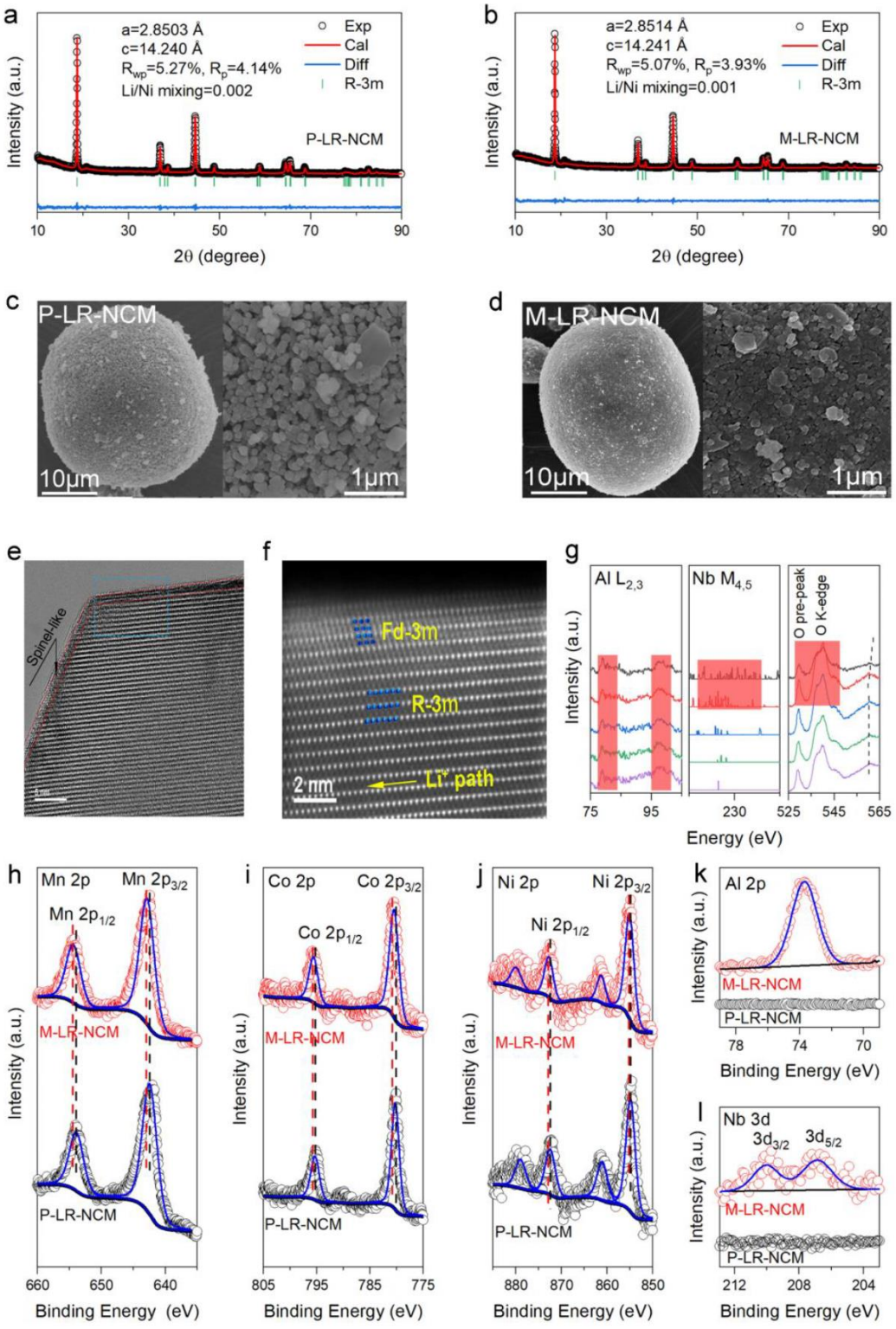

Figure 1. (a) P-LR-NCM and (b) M-LR-NCM Rietveld refinement XRD results through FullProf, SEM images of (c) P-LR-NCM and (d) M-LR-NCM, (e) HRTEM image of M-LR-NCM and (f) corresponding HAADF-STEM image of the blue rectangle area, (g) EELS spectra profiles from the surface (black) to the interior (purple) of M-LR-NCM, comparison of the XPS spectra of (h) Mn 2p, (i) Co 2p, (j) Ni 2p, (k) Al 2p, (l) Nb 3d taken from the P-LR-NCM and M-LR-NCM powder.

the coexistence of Nb and Al in composite surface. Further, the variant atomic concentration of Nb and Al elements during etching (**Figure S7**) suggests an approximately 16 nm average thickness of discontinuous Al_2O_3 layer. Combined with electron paramagnetic resonance (EPR), the O1s fitting results reflect a higher concentration of oxygen vacancies in M-LR-NCM as compared to P-LR-NCM (**Figure S8**).On the basis of all the aforementioned results, this method successfully introduces a

composite surface configuration on the surface and exerts negligible effects on the intrinsic bulk compositions and structures in LR-NCM. To disclose the synergistic effects from the surface structure on the materials, a comprehensive analysis is required to reveal the properties after electrochemical activation.

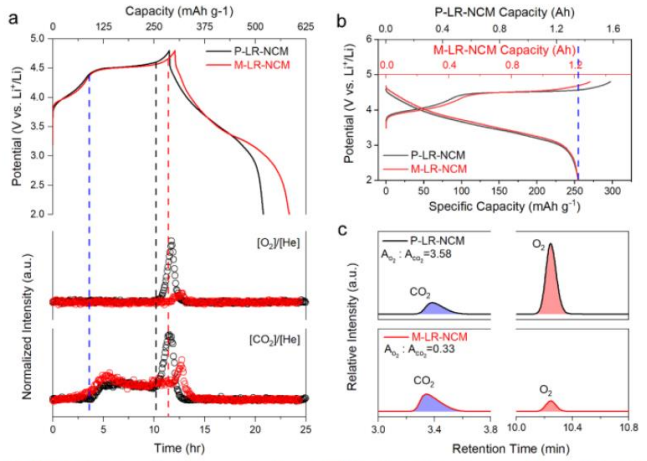

Figure 2. (a) First-cycle charge/discharge profile (top) and the normalized intensity measured by DEMS (bottom) for O_2 and CO_2 of the P-LR-NCM and M-LR-NCM, (b) first-cycle charge/discharge profile from ~1 Ah pouch cells of P-LR-NCM and M-LR-NCM, (c) the corresponding GC results for O_2 and CO_2 derived from P-LR-NCM and M-LR-NCM pouch cells.

Gas release inspection

In this study, both differential electrochemical mass spectrometry (DEMS) and gas chromatography (GC) measurements were used to rate the gas restraint capability for P-LR-NCM and M-LR-NCM in different sets (details are shown in Experiment section and **Figure S9**). As shown in **Figure 2**a, the O_2 gas is appeared at the end of O plateau, while the CO_2 gas is exhibited at the beginning of O plateau. As for CO_2, both samples show the similar release behavior at about 4.4 V, which is mainly caused by the decomposition of carbonate electrolyte.[9] As indicated above, once O_2 starts to release, a sharp peak simultaneously emerges in CO_2, validating the trigger effects of O_2 on side reactions with electrolytes. Turning to O_2, apparently, M-LR-NCM has a dramatically reduced amount of O_2 release as compared to P-LR-NCM. Meanwhile, the starting point of releasing oxygen for M-LR-NCM is 4.67 V, which is 0.07 V higher than that of P-LR-NCM. The restricted oxygen release behavior benefits from the contribution of strong metal-O bonds along with the increased partial oxygen pressure.[12-15] Expectedly, the mobility of active oxygen ions is significantly hindered following with disturbed dimerization of oxygen ions. Thus, there is no doubt that M-LR-NCM has a better O_2 gas restraint capability than P-LR-NCM. To simulate an ambient close to reality and further qualitatively analysis the respective contribution of CO_2 and O_2 to entire released gas, a 10 µL gas from two samples with similar capacity in pouch cells was collected under Ar atmosphere. As shown in **Figure 2**b, though the capacity is slightly different for two samples, the specific capacity is almost equal at 0.1C, indicating an unrestricted electrochemical behavior for both samples. All different gases with the distinguished retention time are involved in GC profile (**Figure S10**). It is worth pointing out that the parallel tests are identical to respective results. And the N_2 emerged in GC profile is already discussed in the previous paper,[36] which does not have any influences on this analysis. As for P-LR-NCM, a prominent O_2 peak at 10.2 - 10.4 min with relatively low CO_2 content at 3.2 - 3.6 min in **Figure 2**c, displays the regular gas release issue in LR-NCM positive electrode materials. In contrast, much less O_2 is emerged for M-LR-NCM after surface modification. Since the CO_2 evolution in both samples has relatively close intensities as shown in **Figure S10**, a qualitatively analysis on individual contribution of CO_2 and O_2 in the entire gas could be quantified by regarding the content of CO_2 as a reference. Consequently, the integrated area ratio for the major gas (A_{O2}:A_{CO2}) decreases significantly from 3.58 to 0.33 after introducing our surface method, thus, giving powerful evidence that a composite surface configuration with desired structures provides remarkable restraint against gas release.

Structural evolution of the composite surface

The majority of gas evolution was completed after first cycle activation, accompanying with the decomposition of carbonate electrolytes and the generation of oxygen radicals.[8] The drastically changed electrode/electrolyte interface further triggered considerable side reactions. As indicated in the previous report,[8, 37] those side reactions were devoted to forming an amorphous layer on the surface of P-LR-NCM and propagating the phase transition from surface to bulk. Lurking in the TEM images, the different structural evolution of M-LR-NCM was propitious to disclose the protecting mechanism of the composite surface. As shown in **Figure 3**a and e, the HRTEM images clearly display a non-uniform surface at the edge of M-LR-NCM without any amorphous layers. The distinct phenomenon is ascribed to distinguished gas restraint ability of M-LR-NCM. Since the oxygen ions are hardly extracted from the M-LR-NCM, there are negligible oxygen radicals participating in

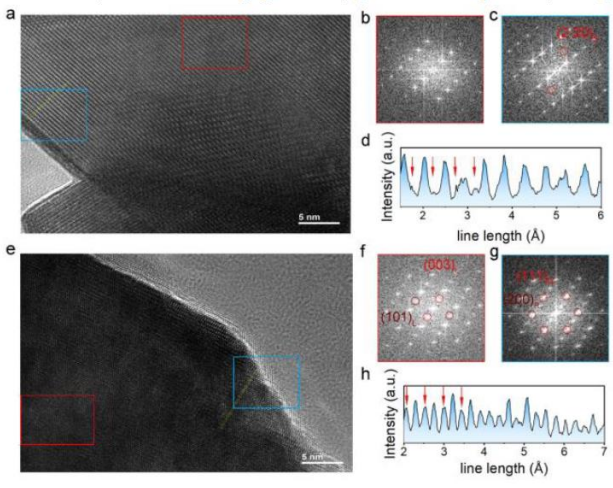

Figure 3. (a) HRTEM image of M-LR-NCM before cycling, the corresponding FFT patterns of (b) red rectangle area (center), (c) blue rectangle area (edge), and (d) the related line intensity profile of yellow line from edge to center. (e) HRTEM image of M-LR-NCM after cycling, the corresponding FFT patterns of (f) red rectangle area (center), (g) blue rectangle area (edge), and (h) the related line intensity profile of yellow line from edge to center. The red arrows in (d) and (h) indicate the line intensity in Li sites.

the formation of amorphous layers. Expectedly, the center of the electrode is untouched and maintained in a layer structure, which is verified through related fast Fourier transform (FFT) patterns (**Figure 3**b and f). Instead, the structure of the non-uniform surface on the edge is significantly transformed. **Figure 3**g exhibits strengthen $(111)_R$ and $(200)_R$ with weaken $(101)_L$ and $(003)_L$ as compared to **Figure 3**f. The transformed FFT patterns suggest the composite surface is converted to a rocksalt structure from a spinel structure (**Figure 3**c).[38] Since the line intensity reflects the amounts of TM ions, the intensity growth of TM ions in Li sites reveals that the TM migration is exacerbated after cycling (**Figure 3**d and h). It is important to note that the TM migration only occur on the near-edge of M-LR-NCM, which is confirmed by the gradual intensity decline of TM ions in Li sites along with the increase of line length. The limited phase transitions are also benefited from the retarded mobility of oxygen ions, which results to reduced side reactions with finite HF attack. With the strengthen stability of surface structure, M-LR-NCM mitigates a wide spread phase transition at the expense of completely converting near-edge structures to the rocksalt structure. Besides, it should be noted that the complete transformation would not enforce the lattice distortion as the expansion of *c*-axis is alleviated as shown in **Figure S11**. Specifically, P-LR-NCM undergoes 0.80 % expansion, while that is 0.61% for M-LR-NCM. Further, P-LR-NCM expands from 100.305 to 102.233, the lattice expansion is 1.92 %. However, M-LR-NCM only expands 1.88 % after first cycle. The mitigated lattice expansion at first cycle revealed the enhanced structural stability of M-LR-NCM due to reduced oxygen evolution. Though the rocksalt structure is not conducive to the migration of Li ions, the limited phase transition, confirmed in following discussion, greatly contributes to the preservation of the diffusion path for Li ions. Combined with the sufficient activation of oxygen ions, it can be inferred that a steady electrode/electrolyte interphase and non-interrupt O redox are guaranteed for M-LR-NCM, further ensuring the electrochemical performance of M-LR-NCM during cycling.

Electrochemical properties

To evaluate the composite surface structure on the cycling performance, a series of electrochemical measurements were carried out. Because of the detected oxygen release phenomenon, a narrower potential window of 2.0 to 4.6 V *vs*. Li^+/Li was applied to avoid the major influence that came from released oxygen and optimize the cycling stability for both samples.[37] However, the first-cycle electrochemical performances of both samples under upper cut-off potential at 4.8 V *vs*. Li^+/Li are still given in **Figure S12**. Both samples exhibit typical redox characteristics.[39] The M-LR-NCM electrode delivers the higher discharge capacities of 280 mAh g^{-1} at 25 mA g^{-1}, which is 11 mAh g^{-1} higher than that of P-LR-NCM. **Figure 4**a shows the initial charge-discharge curves from 2.0 to 4.6 V *vs.* Li^+/Li at room temperature (25 ˚C) with the same specific current. Specifically, the initial discharge capacity of M-LR-NCM is 268 mAh g^{-1}, which is higher than 257 mAh g^{-1} for P-LR-NCM. Besides, a 94.5% initial coulombic efficiency of M-LR-NCM is achieved with the participation of the composite surface configuration, suggesting a higher reversibility of oxygen redox as compared to P-LR-NCM (88.2%). A reasonable origin of the high initial coulombic efficiency lies in two aspects: first, the doped ions induced inert surface oxygen ions, which retards the irreversible charge capacity;[12] secondly, an extended discharge capacity is achieved due to the formation of spinel-like structure at around 2.8 V *vs.* Li^+/Li.[13, 40] Additional investigation (**Figure S13**) confirms the improvement is originated from doping and oxygen vacancies. Because the initial columbic efficiency is promoted to 90.4% of sample without Al_2O_3 coating as compared to 85.2 % of P-LR-NCM. Furthermore, although the sample without coating has similar initial columbic efficiency with M-LR-NCM, the promoted intercalation of Li ions, 15 mAh g^{-1} particularly, is affected by enhanced surface integrity after Al_2O_3 coating. The related cyclic voltammetry (CV) measurements on first charge/discharge cycling are plotted in **Figure 4**b. At the scan rate of 0.1 mV s^{-1}, the curves are close to the galvanostatic conditions under 25 mA g^{-1}. A higher shift in the TM and O oxidation peak with reduced oxygen oxidation peak intensity indicates the promoted valence of transition metal ions confirmed in above XPS results and pre-activated Li_2MnO_3 caused by oxygen vacancies.[13] As for reduction peak, the higher shift and reduced intensity at 3.8 V *vs.* Li^+/Li suggests a reserved TM valence evolution, which mitigates TM migration during cycling.[41, 42] As the potential moving towards the negative potential end, a reduction peak of 2.85 V *vs.* Li^+/Li is clearly found, which is assigned to the spinel-like structure.[40] **Figure S14**a displays the paired oxidation peak of spinel-like phase at around 3 V *vs.* Li^+/Li and following three cycles performance for M-LR-NCM. Different from P-LR-NCM (**Figure S14**b), the gentler curve evolution of M-LR-NCM electrode elucidates the improved structural stability after surface modification with highly reserved oxygen redox. Surprisingly, the contribution from TM oxidation and O oxidation is different for P-LR-NCM and M-LR-NCM during first charging process (**Figure 4**c). The capacity derived from TM oxidation significantly decreased from 129 to 108 mAh g^{-1} in M-LR-NCM implies a reduced amount of oxidable TM ions in M-LR-NCM, such as $Ni^{2+/3+}$ and Co^{3+}. As indicated above, the TM dissolution during synthesizing and promoted valences of TM ions are believed to account for the reduction. An enhanced O oxidation contribution in M-LR-NCM is confirmed after calculating the capacity at high potential (> 4.45V *vs.* Li^+/Li),[43] which increases from 162 to 176 mAh g^{-1}.

To gain insights into the diffusion coefficient of Li ions in the first cycle, a galvanostatic intermittent titration technique (GITT) measurement was taken at an extremely low current rate of 10 mA g^{-1} (**Figure S15**). A large overpotential observed in the charge plateau (> 4.45 V *vs.* Li^+/Li) and discharge region (< 3.5 V *vs.* Li^+/Li) indicates that the Li^+ ions are kinetically limited during extraction and insertion. The Li^+ diffusion coefficient can be calculated by the Fick's second law as **Equation 1** (see in Experiment section). Regardless of taking the thickness of electrode into consideration, **Figure 4**d integrates calculated results and displays differential behaviors of P-LR-NCM and M-LR-NCM in four specific regions: initially, it can be seen that M-LR-NCM has a larger $D_{Li}+/R^2$ than P-LR-NCM at first low potential

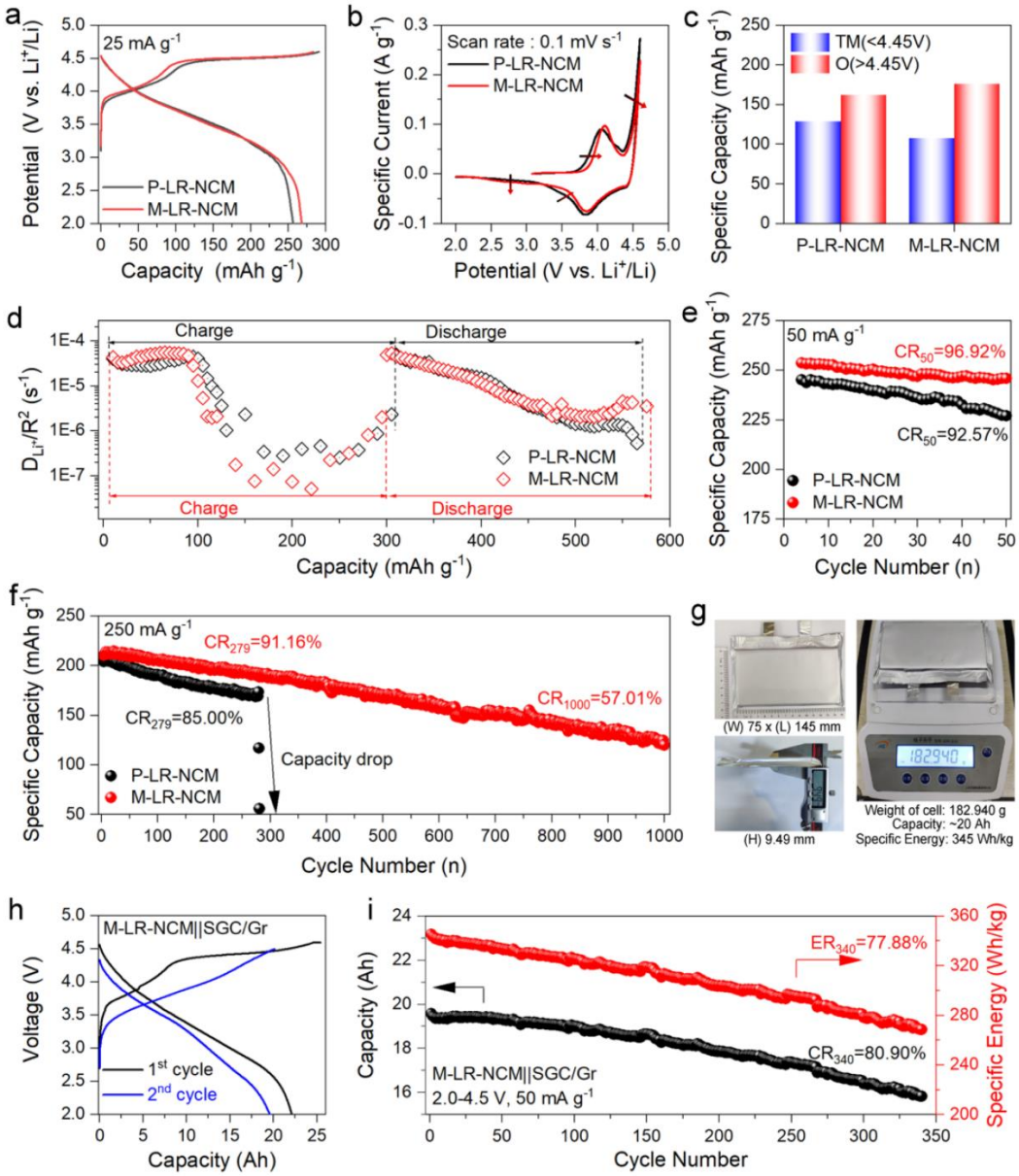

Figure 4. (a) The initial charge/discharge profiles, (b) CVs for the initial cycle, (c) the contribution from TM and O redox in first charging process, (d) the diffusion coefficient of Li ions calculated from the GITT curves, the cycling performance at (e) 50 mA g^{-1} and (f) 250 mA g^{-1} at room temperature. (g) Photos of M-LR-NCM||SGC/Gr pouch cell. (h) The charge/discharge profiles at initial two cycles of M-LR-NCM||SGC/Gr pouch cell. The 1st cycle is the formation cycle at 2.0-4.6 V at 25 mA g^{-1}; the 2nd cycle is regular cycle at 2.0-4.5 V at 50 mA g^{-1}. (i) The discharging capacity and specific energy of the pouch cell tested at 2.0-4.5 V at 50 mA g^{-1} over long cycling.

charge region, suggesting a promoted Li ions extraction during TM oxidation. Secondly, owing to the strong metal-O bonds at the surface, the $D_{Li}+/R^2$ of M-LR-NCM experiences a minor reduction at oxygen oxidation region. As discussed in the previous papers,[6, 44, 45] since defects such as oxygen vacancies and holes are likely to form after oxygen release, and facilitate the Li ions diffusion with reduced energy barrier, a relatively low $D_{Li}+/R^2$ implies a well-preserved surface in M-LR-NCM without forming uncontrolled defects. Thirdly, at the high potential discharge region, a reduced $D_{Li}+/R^2$ of M-LR-NCM indicates a restricted reduction of TM ions, which is the main representation of TM migration. Finally, at the low potential discharge region, $D_{Li}+/R^2$ of M-LR-NCM is significantly improved with the assistance from spinel-like phase. In contrast, P-LR-NCM undergoes a severe structural transformation caused by aforementioned TM migration, greatly hindering the diffusion of Li ions. Thus, a self-regulated Li-ion diffusion that relies on the participation of doping layer and oxygen vacancies is confirmed from the related electrochemical performances in the first cycle. The composite surface configuration exerts a synergistic effect on LR-NCM positive electrode materials by preferentially facilitating reversible electrochemical process and mitigating detrimental phase transition.

Regarding to cycling stability, different current rates were applied in order to detect the capacity fade phenomenon over long cycles. The capacity retention for M-LR-NCM is 96.9% over 50 cycles at 50 mA g^{-1} (**Figure 4**e), and 91.2% after 150 cycles at 125 mA g^{-1} (**Figure S16**), which are greater than 92.6% and 90.5% for P-LR-NCM, respectively. Once tested at 250 mA g^{-1} for a long period cycling, as shown in **Figure 4**f, it is observed that

P-LR-NCM has more serious deteriorating rate than M-LR-NCM. In addition, a suddenly steep capacity drop is originated for P-LR-NCM at 279th cycle. In fact, there are abundant P-LR-NCM samples in this study experiencing a serious charging issue once prolong them to 300 cycles, though the cut-off potential was reduced to decelerate the structure degradation of P-LR-NCM. The possible cause is thought to be the thick carbonated solid electrolyte interface (SEI) formed from side reactions between materials surface and electrolytes.[8] Once the lithiophobic SEI without rational design self-generates to critical extent, it will definitely hinder the exchange of Li ions and accelerate the consumption of Li ions from electrolytes, resulting to a cliff-like drop in discharging capacity and die in following several cycles. In comparison, M-LR-NCM exhibits a highlighted cycling stability over extremely long period cycling for 1000 cycles. To be specific, M-LR-NCM not only exhibits a better capacity retention, *i.e.,* 91.2% at 279th cycle as compared to 85.0% for P-LR-NCM, but also retains its 57.0% capacity at the end with a steady capacity fade of just 0.091mAh g^{-1} per cycle. However, as shown in **Figure S17**, the corresponding potential decay of M-LR-NCM is severer than P-LR-NCM. The discharging potential at 279th cycles is only retained 89.8% of initial potential at 250 mA g^{-1}, while that of P-LR-NCM is 92.7%. A likely assumption is that the composite surface suppresses O_2 release in M-LR-NCM, resulting to caged O_2 in bulk. Those oxygens are still available to redox during cycling, facilitating the oxygen redox during cycling.[46] The fast capacity fade of solely Al_2O_3 coated LR-NCM (**Figure S18**) further complements this assumption. Owing to the enhanced surface integrity, mobile oxygen ions are likely to transport through oxygen vacancies from bulk to surface without the strong Nb-O bonding. As the trapped molecular oxygen reduces, the reversible O redox is accordingly attenuated. On the contrary, more O_2 reserved in bulk contributes to the reversibility of oxygen redox over the entire life-span, though the potential decay is deteriorated due to accumulated potential hysteresis from reversible O redox.[47] It should be pointed out that though the potential decay is severer in M-LR-NCM, the specific potential decay is only 1.2 mV per cycle between the first and the 279th cycle, which is comparable with previous paper.[48-50] In addition to the potential decay, the achieved electrochemical performances are also decent and found comparable with current reports as shown in **Figure S19** and **Table S3**. The thermal stability of P-LR-NCM and M-LR-NCM in charging states is measured as shown in **Figure S20**. In addition to the delayed exothermic temperature from 231.2 to 253.3 ˚C, M-LR-NCM also has a reduced specific heat generation from 1359.0 to 940.2 J g^{-1} with the participation of electrolytes. Those results both demonstrate the promoted thermal stability after the surface modification. Nevertheless, an improved rate capability is also detected as shown in **Figure S21**, suggesting a facile Li ions kinetics contributed from 3D Li ions diffusion channels and integrated surface without thick SEI.

To verify the availability of this method in practical employment, large-capacity practical pouch cells with pre-lithiated SGC/Gr (SiO/Graphene/pitch-pyrolytic mixed with graphite) negative electrodes were fabricated (see details in Experiment section, **Figure 4**g and h). The discharge capacity and corresponding specific energy of M-LR-NCM upon cycling in full cells at 50 mA g^{-1} are plotted in **Figure 4**i. Regardless of the formation CC-CV cycle, M-LR-NCM can deliver an ultrahigh specific energy of 345 Wh kg^{-1} with 19.6 Ah discharge capacity at normal working voltage. Subsequently, M-LR-NCM retains 77.9% specific energy at 268.7 Wh kg^{-1} after 340 cycles, whereas the discharge capacity is 15.8 Ah at 80.9% capacity retention. Such an excellent long cycling performance in full cells with high capacity provides persuasive evidence that the proposed method is effectively promoting the electrochemical performance of LR-NCM electrodes even under commercial-level practical employment.

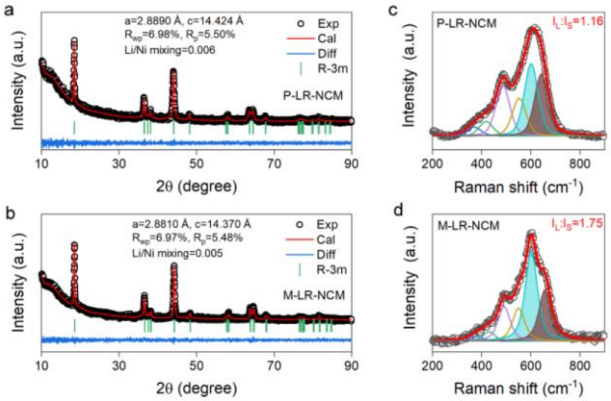

Figure 5. (a) P-LR-NCM and (b) M-LR-NCM Rietveld refinement XRD results through FullProf after 200 cycles at 1C, Raman spectra with fitting results of (c) P-LR-NCM and (d) M-LR-NCM after 200 cycles.

Post-cycling materials investigation

To comprehensively understand the effects of the composite surface modification during cycling, a series of characterizations were conducted to unravel the structure and surface evolution of P-LR-NCM and M-LR-NCM after 200 cycles at 250 mA g^{-1}. As seen from the Rietveld refinement XRD results in **Figure 5**a and b, both samples accomplish the fully activation of Li_2MnO_3 identified by the disappeared $LiMn_6$ superlattice. As a result, both lattice parameters *a* and *c* exhibit lattice expansion. In detail, lattice *a* increases to 2.8890 Å for P-LR-NCM as compared to 2.8810 Å for M-LR-NCM, while lattice *c* extends to 14.424 Å for P-LR-NCM as compared to 14.370 Å for M-LR-NCM. A slightly severe Li/Ni mixing is also detected in P-LR-NCM. Combined with the significantly increased strain (**Table S4**), the aforementioned results indicate a grievous phase transition from layer to spinel/rocksalt due to TM migration in P-LR-NCM. On the contrary, those detrimental phase transition is relatively mitigated for M-LR-NCM, which is also confirmed from the limited increments of spinel phase in M-LR-NCM via double-phase refinement as shown in **Figure S22**. Additional Raman fitting analysing were carried out and exhibited as **Figure 5**c and d. After integrating intensity of the M-O stretching modes at 600 cm^{-1} and 660 cm^{-1}, respectively, the ratio of long to short M-O bonds (I_L : I_S) is much higher in M-LR-NCM, 1.75 as compared to 1.16 in P-LR-NCM. The lower integrated intensity ratio of long to short M-O bonds suggests more surface structures transformed into spinel/rocksalt from layer during cycling. In spite of M-LR-NCM contains more short M-O bonds

in advance as mentioned above (**Figure S2**), a limited decline in $I_L : I_S$ ratio implies a strong resistance to surface phase transition in M-LR-NCM with the assistance of our composite surface configuration.

Subsequently, XPS of P-LR-NCM and M-LR-NCM electrodes after cycling were detected and fitted to disclose the detailed information of side reactions happened between electrodes and electrolytes during cycling. As shown in **Figure 6**a, although the formation of SEI reduced the signal qualities of Mn 2p spectra, the intensity of satellite peak of Mn^{2+} ($2p_{sat}$ 646.8 eV) is slightly raised in P-LR-NCM as compared to M-LR-NCM, indicating the dissolution of manganese oxides in the SEI caused by electrolyte corrosion.[51] Moreover, a considerable shift towards low binding energy in P-LR-NCM suggests the reduced chemical valence from Mn^{4+} to Mn^{3+}, which is ascribed to TM migration. In contrast, M-LR-NCM preserves a higher valence of Mn after 200 cycles, elucidating the reduced side reactions and mitigated TM migration after the surface modification. The unexpected rise at nearly 650 eV for M-LR-NCM may represent the changed surface consists of aluminium manganese oxides.[52] Furthermore, **Figure 6**b-d show the C 1s, F 1s and O 1s spectra of P-LR-NCM and M-LR-NCM electrodes. The whole change provides clear evidence on the formation of SEI via comparing with those spectra before cycling (**Figure S23**a-c). As shown in **Figure 6**b, it can be speculated that a reduced peak intensity for C-C bond at 284.6 eV, increased peak intensities for C-H bond at 285.0 eV, C-O bond or CH_2 in PVDF at 286.2 eV and O-C-O or O-C=O bond at 287.6 eV, and a shifted peak from CO_3^{2-} or PVDF at 290.3 eV to $ROCO_2Li$ at 290.1 eV for P-LR-NCM. The evolution in C 1s spectra indicates the decomposition of electrolyte and the formation of a carbonate surface films that consists of $ROCO_2Li$ and other carboxylic group species are serious in P-LR-NCM,[53] yet the M-LR-NCM shows a great resistance against side reactions. As for F 1s (**Figure 6**c), an intense component at 685.0 eV is ascribed to LiF. The significant growth on LiF intensity indicates the serious HF attack originated from side reactions between electrolytes and positive electrodes.[8] The appearance of PF_xO_y peak at 687 eV illustrates the decomposition of $LiPF_6$.[53] Thus, a catastrophically changed surface and over consumption of electrolytes during cycling are both verified in P-LR-NCM. Under this circumstance, there is no doubt that P-LR-NCM experiences a sudden capacity drop in long period cycling. By contrast, the whole peaks in M-LR-NCM could be deconvoluted to a main peak at PVDF (~688 eV),[53] limited Al-F approximately at 685.5 to 686.5 eV,[54] and a slight raised peak of LiF. Though there is no obvious peak related to Al-F emerged in F 1s spectra, the slight shift of PVDF peaks towards lower binding energy suggests the formation of Al-F bond, indicating the defense against HF attack from Al_2O_3 surface.

To get a deeper insight into the SEI formation, Ar sputtering was employed to investigate the most informative part, O 1s. Before sputtering, O 1s spectra (**Figure 6**d) in P-LR-NCM is dominated by $ROCO_2Li$ at 533.5 eV and CO_3^{2-} at ~532.0 eV without any intensity of lattice oxygen at 529.7 eV and Al-O-F at 532.7 eV exhibited in M-LR-NCM O 1s spectra.[53] The disappeared lattice oxygen peaks in P-LR-NCM indicate a reduced oxygen activity at the surface, which is ascribed to the oxygen release with

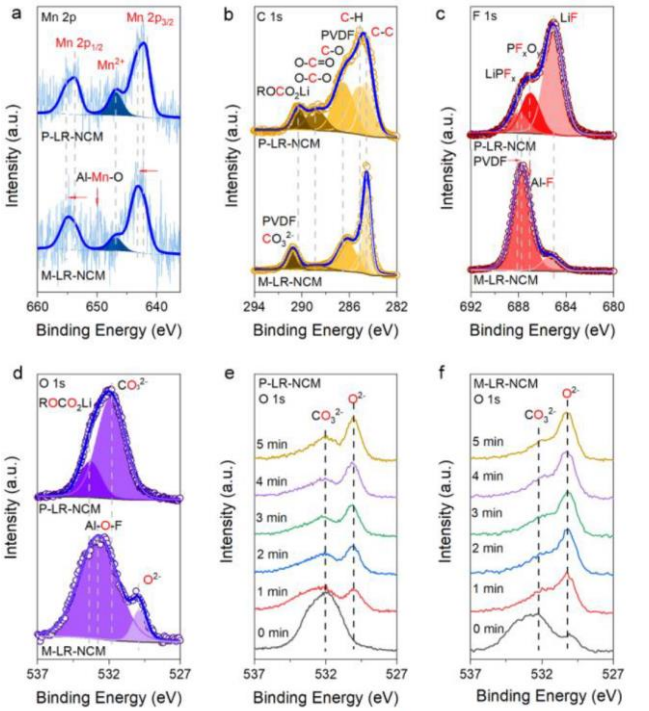

Figure 6. Comparison of the XPS spectra of (a) Mn 2p, (b) C 1s, (c) F 1s and (d) O 1s of the P-LR-NCM and M-LR-NCM after 200 cycles. O 1s XPS spectra according to sputtering time of (e) P-LR-NCM and (f) M-LR-NCM.

affected surface stability during cycling. As long as the oxygen radicals contacts with electrolytes, the triggered side reactions form thick SEI consisting of abundant carbonate and organic species around surface, which further degrades the intensity of lattice oxygen. On the opposite, the reduced carbonate and organic species intensities show the robustness of the modified surface without reacting with electrolytes. Surprisingly, the peak of lattice oxygen is still retained under the protection from the composite surface, which is regarded as the origin of highly reversible oxygen redox. By taking advantage of the protection of Al_2O_3, HF is scavenged and Al-containing oxyfluorides are formed as SEI. Though both samples formed SEI during cycling, the composition and thickness of SEI are varies from the different generation process. The sputtering was employed to recognize the thickness of SEI. As shown in **Figure 6**e and f, two peaks are emerged: lattice oxygen locates at 529.7 eV and the carbonate species lay at ~532 eV. In accordance with the gradually decreased CO_3^{2-} peaks, the intensity of lattice oxygen is simultaneously increased with the increased sputtering time in P-LR-NCM. As mentioned above, the formation of SEI will further reduce the signals of lattice oxygen. The evolution in P-LR-NCM illustrates a relatively thick SEI layer without eliminating even after 5 min Ar sputtering. However, M-LR-NCM shows an outstanding lattice oxygen peak with broaden carbonate peaks after 2 min sputtering, which confirms that M-LR-NCM has a relatively thin SEI. Concluding XPS results mentioned above, it can be stated here that a relatively thin and desired SEI was formed during cycling with the participation of the composite surface structure. Overall, the composite surface layer contributes to the LR-NCM in a desired circumstance: firstly, it prevents oxygen release during first cycle, which

prevents severe side reactions and electrolyte corrosions in advance; secondly, the mitigated phase transition of the electrode surface without thick carbonate SEI layers ensures a steady Li^+ ions transport between electrodes and electrolytes; last but not least, the lattice oxygen is highly active during cycling, which facilitates the reversibility of oxygen redox during prolonged cycling and further succeeds in high capacity retention for LR-NCM.

Conclusions

In summary, this study has realized a promising cycling stability in LR-NCM by introducing a rationally designed surface structure. The function of each component in this composite surface configuration is verified *via* characterization on the whole electrochemical procedure of modified samples including pre-cycling and post-cycling. Consequently, M-LR-NCM sample offers the improved long cycling stability with a superior capacity fade rate of 0.091 mAh g^{-1} per cycle, which confirms the significance of mitigating gas evolution, especially the oxygen gas, on improving performance of LR-NCM positive electrodes. Moreover, it is appreciated that 345 Wh kg^{-1} commercial-level pouch cells are achieved from M-LR-NCM and SGC/Gr with prolonged cycling. The functionality and reliability of composite surface configuration is further proved under such realistic circumstance. Therefore, this work proposed a practical solution to capitalize promising LR-NCM positive electrodes on high energy LIBs.

Author Contributions

Zhepu Shi and **Qingwen Gu** contributed equally to this work. **Zhepu Shi**: Methodology, Investigation, Formal analysis, Writing-Original Draft; **Qingwen Gu:** Methodology, Resource, Validation; **Liang Yun:** Methodology, Investigation**; Zhining Wei:** Methodology, Validation**; Di Hu:** Writing-Review & Editing; **Bao Qiu:** Conceptualization, Supervision, Writing-Review & Editing; **George Zheng Chen:** Writing-Review & Editing, Supervision**; Zhaoping Liu:** Conceptualization Supervision, Writing-Review & Editing**.**

Conflicts of interest

There are no conflicts to declare.

Acknowledgements

Z.S. acknowledges Doctoral Training Partnership programme provided by University of Nottingham Ningbo China and Ningbo Institute of Materials Technology & Engineering, Chinese Academy of Sciences. This work was supported by the National Natural Science Foundation of China (*Grant No.* 21773279), Natural Science Foundation of Ningbo (*Grant No.* 202003N4030), and S&T Innovation 2025 Major Special Program of Ningbo (*Grant No.* 2018B10081).

Notes and references

1. M. M. Thackeray, S.-H. Kang, C. S. Johnson, J. T. Vaughey, R. Benedek and S. A. Hackney, *J. Mater. Chem.*, 2007, **17**, 3112-3125.
2. H. J. Yu and H. S. Zhou, *J. Phys. Chem. Lett.*, 2013, **4**, 1268-1280.
3. A. Manthiram, J. C. Knight, S. T. Myung, S. M. Oh and Y. K. Sun, *Adv. Energy Mater.*, 2016, **6**, 1501010.
4. G. Assat and J. M. Tarascon, *Nat. Energy*, 2018, **3**, 373-386.
5. B. Li and D. G. Xia, *Adv. Mater.*, 2017, **29**, 1701054.
6. W. Yin, A. Grimaud, G. Rousse, A. M. Abakumov, A. Senyshyn, L. Zhang, S. Trabesinger, A. Iadecola, D. Foix, D. Giaume and J. M. Tarascon, *Nat. Commun.*, 2020, **11**, 1252.
7. I. Belharouak, W. Lu, D. Vissers and K. Amine, *Electrochem. Commun.*, 2006, **8**, 329-335.
8. J. Hong, H.-D. Lim, M. Lee, S.-W. Kim, H. Kim, S.-T. Oh, G.-C. Chung and K. Kang, *Chem. Mater.*, 2012, **24**, 2692-2697.
9. S. A. Freunberger, Y. Chen, Z. Peng, J. M. Griffin, L. J. Hardwick, F. Barde, P. Novak and P. G. Bruce, *J. Am. Chem. Soc.*, 2011, **133**, 8040-8047.
10. W. Zhang, Y. Sun, H. Deng, J. Ma, Y. Zeng, Z. Zhu, Z. Lv, H. Xia, X. Ge, S. Cao, Y. Xiao, S. Xi, Y. Du, A. Cao and X. Chen, *Adv. Mater.*, 2020, **32**, 2000496.
11. X. Zhang, I. Belharouak, L. Li, Y. Lei, J. W. Elam, A. Nie, X. Chen, R. S. Yassar and R. L. Axelbaum, *Adv. Energy Mater.*, 2013, **3**, 1299-1307.
12. S. Liu, Z. Liu, X. Shen, W. Li, Y. Gao, M. N. Banis, M. Li, K. Chen, L. Zhu, R. Yu, Z. Wang, X. Sun, G. Lu, Q. Kong, X. Bai and L. Chen, *Adv. Energy Mater.*, 2018, **8**, 1802105.
13. B. Qiu, M. Zhang, L. Wu, J. Wang, Y. Xia, D. Qian, H. Liu, S. Hy, Y. Chen, K. An, Y. Zhu, Z. Liu and Y. S. Meng, *Nat. Commun.*, 2016, **7**, 12108.
14. X. D. Zhang, J. L. Shi, J. Y. Liang, Y. X. Yin, J. N. Zhang, X. Q. Yu and Y. G. Guo, *Adv. Mater.*, 2018, **30**, 1801751.
15. Z. Zhu, D. Yu, Y. Yang, C. Su, Y. Huang, Y. Dong, I. Waluyo, B. Wang, A. Hunt, X. Yao, J. Lee, W. Xue and J. Li, *Nat. Energy*, 2019, **4**, 1049-1058.
16. X. Ding, D. Luo, J. Cui, H. Xie, Q. Ren and Z. Lin, *Angew. Chem. Int. Ed. Engl.*, 2020, **59**, 7778-7782.
17. H. C. Guo, K. Jia, S. J. Han, H. Zhao, B. Qiu, Y. G. Xia and Z. P. Liu, *Adv. Mater. Interfaces*, 2018, **5**, 1701465.
18. S. Dong, Y. Zhou, C. Hai, J. Zeng, Y. Sun, Y. Shen, X. Li, X. Ren, C. Sun, G. Zhang and Z. Wu, *J. Power Sources*, 2020, **462**, 228185.
19. M. Zubair, G. Li, B. Wang, L. Wang and H. Yu, *ACS Appl. Energy Mater.*, 2018, **2**, 503-512.
20. R. Benedek and H. Iddir, *J. Phys. Chem. C*, 2017, **121**, 6492-6499.
21. P. K. Nayak, J. Grinblat, M. Levi, E. Levi, S. Kim, J. W. Choi and D. Aurbach, *Adv. Energy Mater.*, 2016, **6**, 1502398.
22. A. R. Armstrong, M. Holzapfel, P. Novak, C. S. Johnson, S. H. Kang, M. M. Thackeray and P. G. Bruce, *J. Am. Chem. Soc.*, 2006, **128**, 8694-8698.
23. F. Lin, I. M. Markus, D. Nordlund, T. C. Weng, M. D. Asta, H. L. Xin and M. M. Doeff, *Nat Commun*, 2014, **5**, 3529.
24. G. Assat, C. Delacourt, D. A. Dalla Corte and J. M. Tarascon, *J. Electrochem. Soc.*, 2016, **163**, A2965-A2976.
25. R. Fu, J. Ji, L. Yun, Y. Jiang, J. Zhang, X. Zhou and Z. Liu, *Energy Storage Mater.*, 2021, **35**, 317-326.

26. M. M. Thackeray, S. H. Kang, C. S. Johnson, J. T. Vaughey and S. A. Hackney, *Electrochem. Commun.*, 2006, **8**, 1531-1538.
27. Y. Li, Y. Bai, X. Bi, J. Qian, L. Ma, J. Tian, C. Wu, F. Wu, J. Lu and K. Amine, *ChemSusChem*, 2016, **9**, 728-735.
28. W. He, P. Liu, B. Qu, Z. Zheng, H. Zheng, P. Deng, P. Li, S. Li, H. Huang, L. Wang, Q. Xie and D. L. Peng, *Adv. Sci.*, 2019, **6**, 1802114.
29. M. Okubo, E. Hosono, J. Kim, M. Enomoto, N. Kojima, T. Kudo, H. Zhou and I. Honma, *J. Am. Chem. Soc.*, 2007, **129**, 7444-7452.
30. H. C. Guo, Z. Wei, K. Jia, B. Qiu, C. Yin, F. Q. Meng, Q. H. Zhang, L. Gu, S. J. Han, Y. Liu, H. Zhao, W. Jiang, H. F. Cui, Y. G. Xia and Z. P. Liu, *Energy Storage Mater.*, 2019, **16**, 220-227.
31. M. Gu, A. Genc, I. Belharouak, D. Wang, K. Amine, S. Thevuthasan, D. R. Baer, J.-G. Zhang, N. D. Browning, J. Liu and C. Wang, *Chem. Mater.*, 2013, **25**, 2319-2326.
32. R. Baddour-Hadjean and J. P. Pereira-Ramos, *Chem. Rev.*, 2010, **110**, 1278-1319.
33. Y. K. Sun, S. T. Myung, B. C. Park, J. Prakash, I. Belharouak and K. Amine, *Nat. Mater.*, 2009, **8**, 320-324.
34. B. Wu, X. Yang, X. Jiang, Y. Zhang, H. Shu, P. Gao, L. Liu and X. Wang, *Adv. Funct. Mater.*, 2018, **28**, 1803392.
35. L. O. d. S. B. M.A.B. Gomes, S.C. de Castro, A.J. Damiao *J. Electrochem. Soc.*, 1990, **137**, A3067-A3070.
36. C. Fang, J. Li, M. Zhang, Y. Zhang, F. Yang, J. Z. Lee, M. H. Lee, J. Alvarado, M. A. Schroeder, Y. Yang, B. Lu, N. Williams, M. Ceja, L. Yang, M. Cai, J. Gu, K. Xu, X. Wang and Y. S. Meng, *Nature*, 2019, **572**, 511-515.
37. P. Hou, F. Li, H. Zhang and H. Huang, *J. Mater. Chem. A*, 2020, **8**, 14214-14222.
38. K.-J. Park, J.-Y. Hwang, H.-H. Ryu, F. Maglia, S.-J. Kim, P. Lamp, C. S. Yoon and Y.-K. Sun, *ACS Energy Lett.*, 2019, **4**, 1394-1400.
39. H. Yu, H. Kim, Y. Wang, P. He, D. Asakura, Y. Nakamura and H. Zhou, *Phys. Chem. Chem. Phys.*, 2012, **14**, 6584-6595.
40. L. Ku, Y. Cai, Y. Ma, H. Zheng, P. Liu, Z. Qiao, Q. Xie, L. Wang and D.-L. Peng, *Chem. Eng. J.*, 2019, **370**, 499-507.
41. G. Assat, D. Foix, C. Delacourt, A. Iadecola, R. Dedryvère and J.-M. Tarascon, *Nat. Commun.*, 2017, **8**, 2219.
42. E. Hu, X. Yu, R. Lin, X. Bi, J. Lu, S. Bak, K.-W. Nam, H. L. Xin, C. Jaye, D. A. Fischer, K. Amine and X.-Q. Yang, *Nat. Energy*, 2018, **3**, 690-698.
43. B. Xu, C. R. Fell, M. Chi and Y. S. Meng, *Energ Environ. Sci.*, 2011, **4**, 2223.
44. J. Liu, M. Hou, J. Yi, S. Guo, C. Wang and Y. Xia, *Energy Environ. Sci.*, 2014, **7**, 705-714.
45. D.-H. Seo, J. Lee, A. Urban, R. Malik, S. Kang and G. Ceder, *Nat. Chem.*, 2016, **8**, 692.
46. R. A. House, J.-J. Marie, M. A. Pérez-Osorio, G. J. Rees, E. Boivin and P. G. Bruce, *Nat. Energy*, 2021, **6**, 781-789.
47. J. R. Croy, K. G. Gallagher, M. Balasubramanian, Z. Chen, Y. Ren, D. Kim, S.-H. Kang, D. W. Dees and M. M. Thackeray, *J. Phys. Chem. C*, 2013, **117**, 6525-6536.
48. C. Yin, X. Wen, L. Wan, Z. Shi, Z. Wei, X. Li, Q. Gu, B. Qiu and Z. Liu, *J. Power Sources*, 2021, **503**, 230048.
49. D. Luo, J. Cui, B. Zhang, J. Fan, P. Liu, X. Ding, H. Xie, Z. Zhang, J. Guo, F. Pan and Z. Lin, *Adv. Funct. Mater.*, 2021, **31**, 2009310.
50. W. Guo, C. Zhang, Y. Zhang, L. Lin, W. He, Q. Xie, B. Sa, L. Wang and D. L. Peng, *Adv. Mater.*, 2021, **33**, 2103173.
51. F. Wu, W. Li, L. Chen, Y. Su, L. Bao, W. Bao, Z. Yang, J. Wang, Y. Lu and S. Chen, *Energy Storage Mater.*, 2020, **28**, 383-392.
52. S. L. Chang, J. W. Anderegg and P. A. Thiel, *J. Non-Cryst. Solids*, 1996, **195**, 95-101.
53. Y.-C. Lu, A. N. Mansour, N. Yabuuchi and Y. Shao-Horn, *Chem. Mater.*, 2009, **21**, 4408-4424.
54. J. Xie, A. D. Sendek, E. D. Cubuk, X. Zhang, Z. Lu, Y. Gong, T. Wu, F. Shi, W. Liu, E. J. Reed and Y. Cui, *ACS Nano*, 2017, **11**, 7019-7027.

Supporting Information

A Composite Surface Configuration towards Improving Cycling Stability of Li-Rich Layered Oxide Materials

Zhepu Shi,[a,b] Qingwen Gu,[a] Liang Yun,[a] Zhining Wei, [a,c] Di Hu,[b] Bao Qiu,[a] George Zheng Chen,*[d] and Zhaoping Liu*[a]*

[a]Ningbo Institute of Materials Technology and Engineering, Chinese Academy of Sciences (CAS), Ningbo, 315201, China

[b]Department of Chemical and Environmental Engineering, Faculty of Science and Engineering, The University of Nottingham, Ningbo, 315100, China

[c]School of Chemical Engineering and Technology, China University of Mining and Technology (CUMT), Xuzhou, 221166, China

[d]Department of Chemical and Environmental Engineering, Faculty of Engineering, The University of Nottingham, Nottingham, NG7 2RD, United Kingdom

*Corresponding author E-mail: qiubao@nimte.ac.cn (B. Qiu); george.chen@nottingham.ac.uk (G. Z. Chen); liuzp@nimte.ac.cn (Z. Liu)

Table S1. Results of the Rietveld analysis for P-LR-NCM and M-LR-NCM from FullProf. And related micro-strain analysis from JADE.

Sample	*a*/Å	*c*/Å	*c*/*a*	Li/Ni Mixing	R_{wp}/%	R_p/%	Strain (%)
P-LR-NCM	2.8503	14.240	4.9960	0.002	5.27	4.14	0.201(0.005)
M-LR-NCM	2.8514	14.241	4.9944	0.001	5.07	3.93	0.209(0.004)

Table S2. Materials and corresponding chemical analyses results.

Sample	Li	Ni	Co	Mn	Al	Nb
P-LR-NCM	1.380	0.172	0.171	0.656	0	0
M-LR-NCM	1.348	0.170	0.167	0.660	0.038	0.003

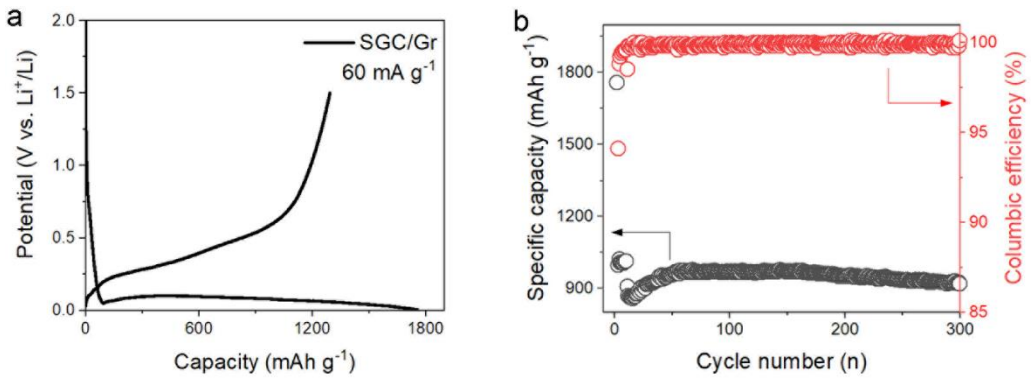

Figure S1. (a) The initial cycle profile of SGC/Gr at 0.05C, (b) the discharge capacity of SGC/Gr at 0.05C in subsequent 300 cycles.

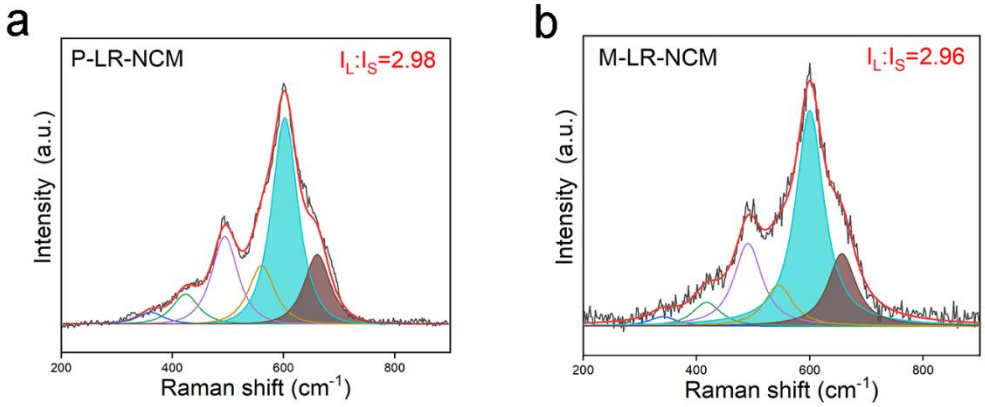

Figure S2. Raman spectra and the fitted results of P-LR-NCM and M-LR-NCM before cycling.

Figure S2 shows the two outstanding sharp peaks appeared at about 500 and 600 cm-1 are characteristic vibration modes of R-3m structure, implying the O-M-O bending (Eg) and M-O stretching (A1g) mode, respectively. The broaden peak existed at the range from 320 to 450 cm-1 reflects the remaining features of Li2MnO3 components. Exclusively, a weak and broad peak about 670 cm-1 for M-LR-NCM is attributed to the formation of spinel-like structure.

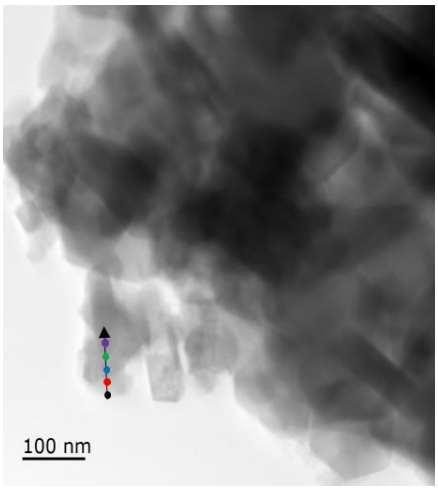

Figure S3. EELS line scan direction from surface (black dot) to bulk (purple dot) in the TEM image. The dots are corresponding to the different location of the scanning line.

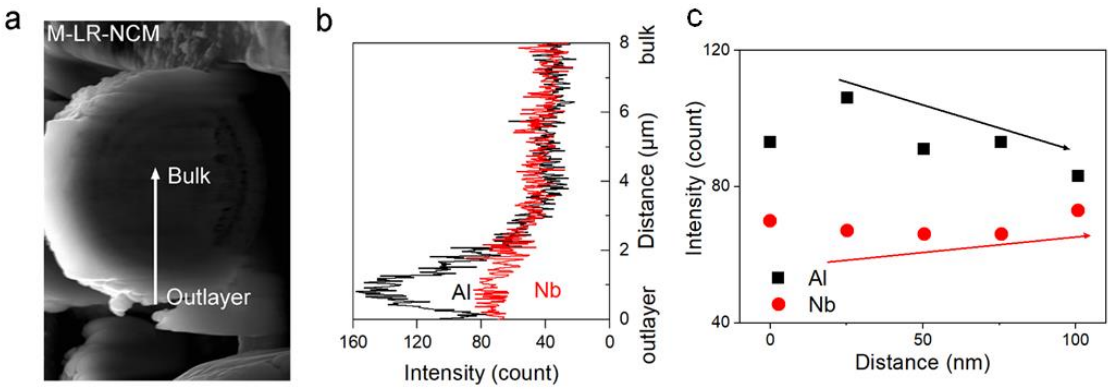

Figure S4. (a) a cross-section image of M-LR-NCM. Arrow indicates the direction of EDX line scan, (b) the corresponding EDX profile of Nb and Al from out layer to bulk along the direction in (a). (c) the enlarged near-surface region of (b).

Figure S4 shows an aggregated concentration of Nb and Al at the surface region from outlayer to 2 μm towards center. After this point, both of them gradually decrease and remain almost constant in the bulk region. At enlarged near-surface region, the gradually reduced intensity of Al indicates the elimination of Al_2O_3 coating and the appearance of doping region once reaching 25 nm.

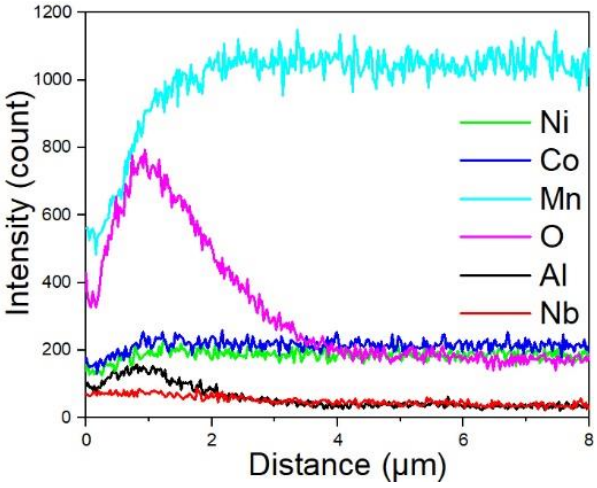

Figure S5. EDX line scan of cross-section M-LR-NCM sample. All elements are involved.

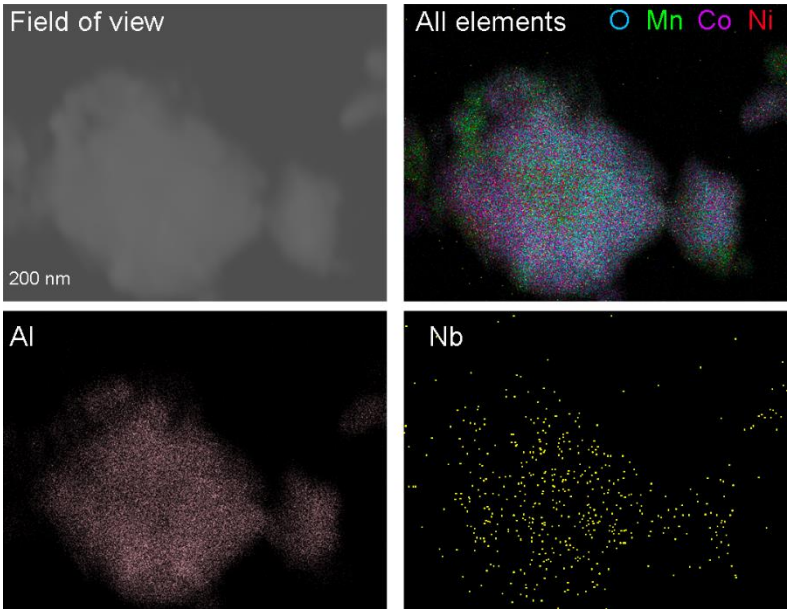

Figure S6. The corresponding EDS mapping of M-LR-NCM from TEM.

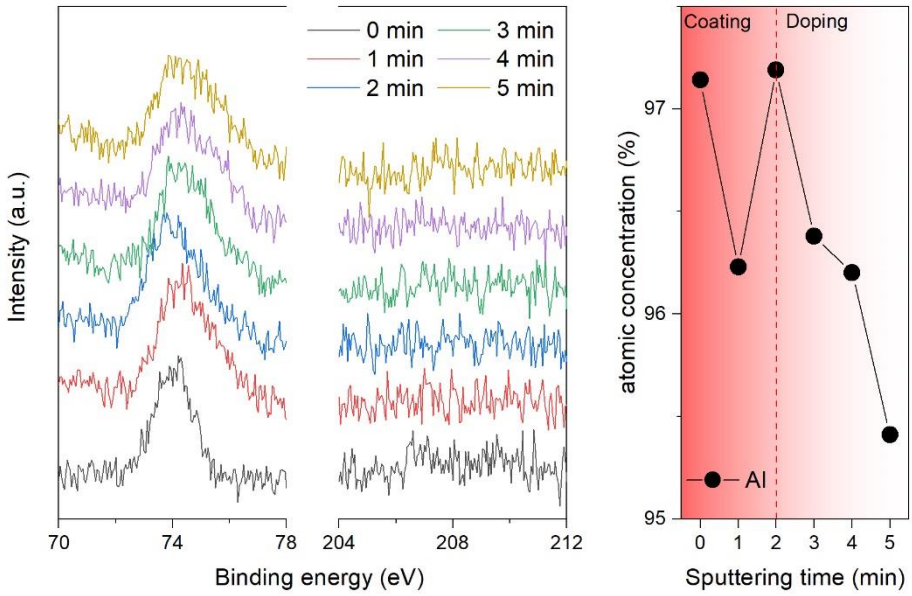

Figure S7. (a) The XPS spectra of Al and Nb during Ar^{+} etching of M-LR-NCM, (b) the variation of corresponding atomic concentration versus the sputtering time based on the comparison between Al and Nb elements.

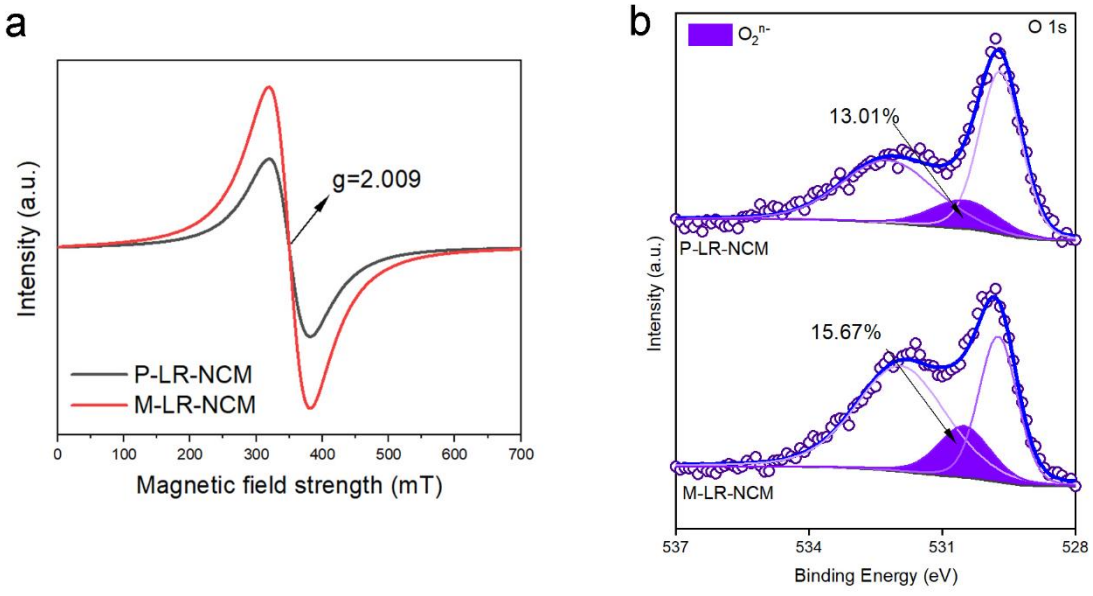

Figure S8. (a) The EPR spectra of both samples, (b) the O 1s fitting results with respective amounts of oxygen vacancies in P-LR-NCM and M-LR-NCM.

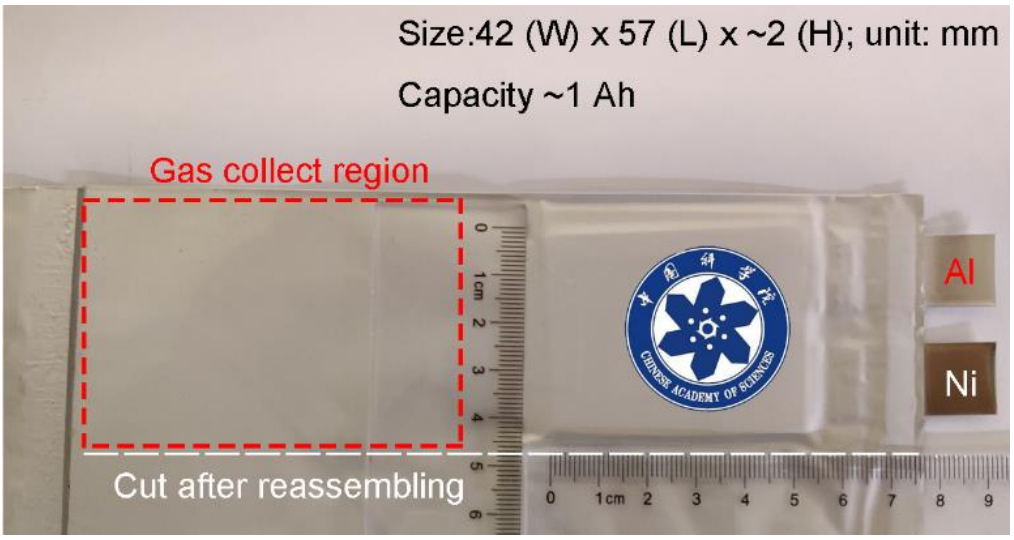

Figure S9. Illustration of home-made ~1 Ah pouch cell designed for GC measurement.

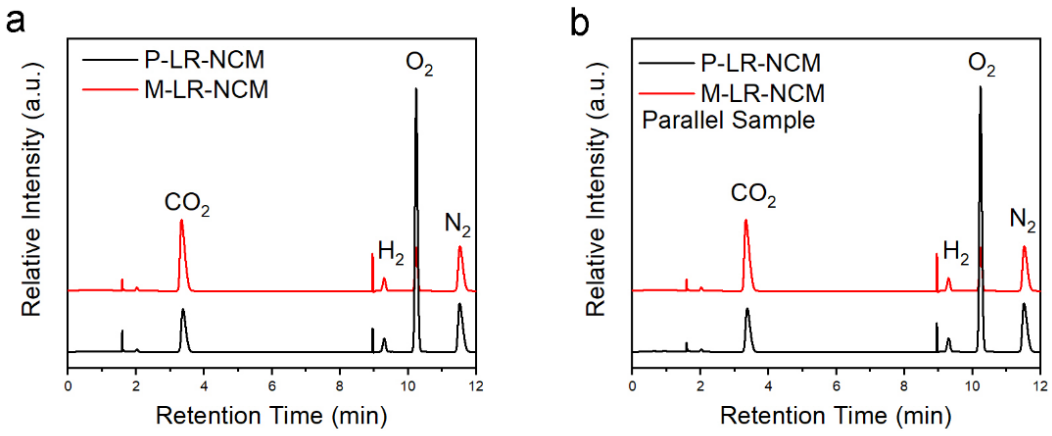

Figure S10. GC profile of gas components collected from the pouch cells after first cycle. (b) Parallel experiments used to verify the results from (a).

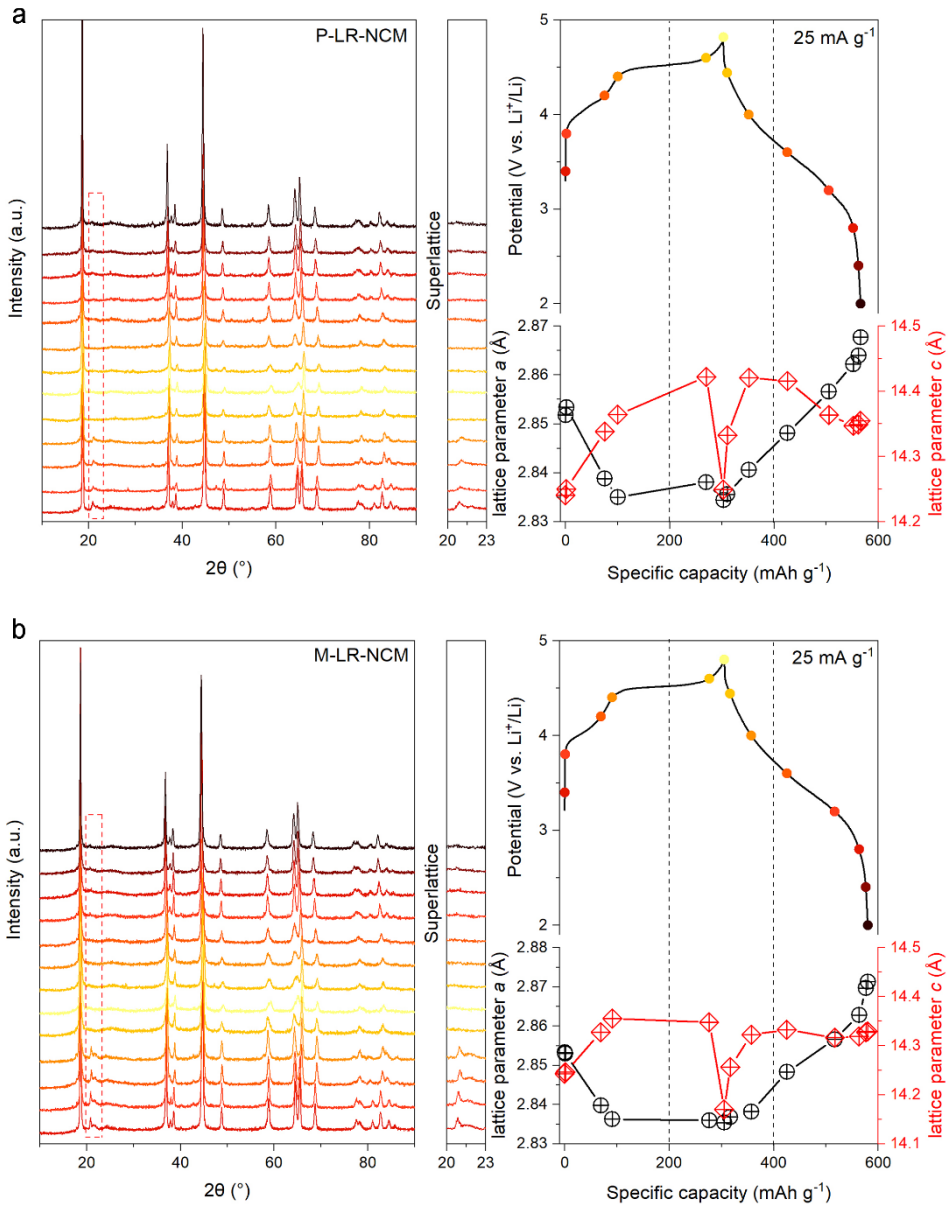

Figure S11. *Ex-situ* XRD results with corresponding lattice parameters of (a) P-LR-NCM and (b) M-LR-NCM at various potential (from left to right, 3.4V, 3.8V, 4.2V, 4.4V, 4.6V, 4.8V at charging; 4.4V, 4.0V, 3.6V, 3.2V, 2.8V, 2.4V, 2.0V at discharging) during first cycle.

As shown in **Figure S11**, the structural evolutions of two samples during first cycle were exhibits. The superlattice structures of both samples were disappeared at 4.6 V, indicating the deintercalation of Li ions from the Li_2MnO_3 domains and activation of O redox. After discharging to 3.2 V, a relatively weak peak reappeared at the position of superlattice structures, which was caused by the intercalated Li ions back to TM layer. However, since the in-plane TM migration disturbed the original arrangement of TM layer,[1] the intensity of superlattice structures was significantly reduced as compared to non-activated one. The similar evolution of superlattice structures illustrated the composite surface configuration would not interrupt the O redox though it exerted positive effects on mitigating gas release. As for the whole structural evolution during first cycle, the corresponding evolution of lattice parameter *a* and *c* suggested a similar behavior

for both samples except the restricted *c* evolution of M-LR-NCM. As for the *c* expansion, P-LR-NCM underwent 0.80 % expansion, while that was 0.61% for M-LR-NCM. The severer expansion of *c* demonstrated the lattice distortion of the host framework.[2] Once it came to the entire volume, P-LR-NCM expanded from 100.305 to 102.233, the lattice expansion was 1.92 %. However, M-LR-NCM only expanded 1.88 % after first cycle. The gas release at first cycle greatly accelerated the structural rearrangement around surface, which further enforced the lattice distortion as the partial frame oxygen ions were lost. The mitigated structural expansion at first cycle revealed the enhanced structural stability of M-LR-NCM due to reduced oxygen evolution.

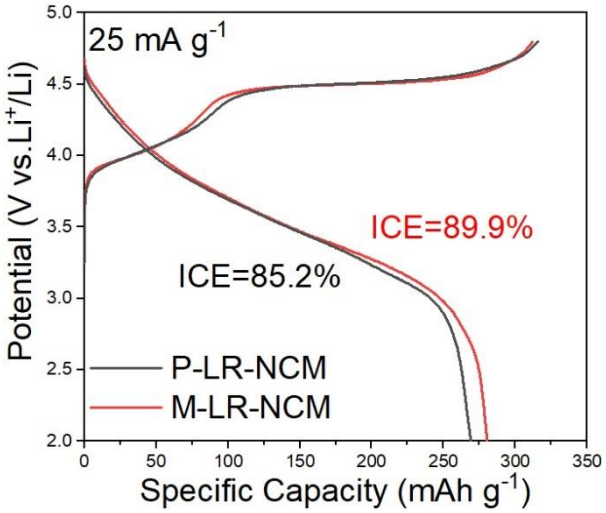

Figure S12. The initial charge-discharge profile of P-LR-NCM and M-LR-NCM at 25 mA g^{-1} between 2.0 to 4.8 V.

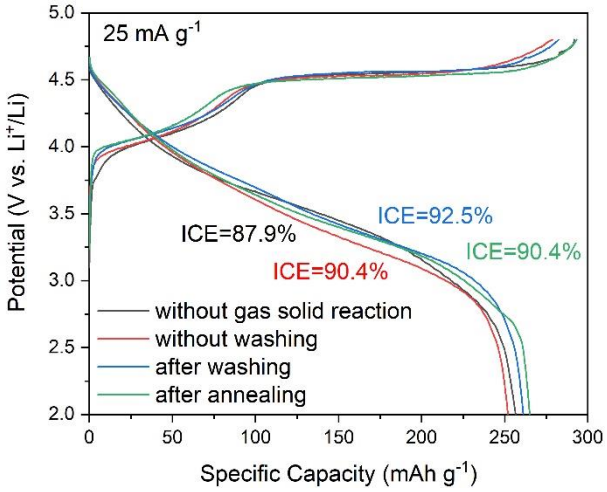

Figure S13. The initial charge-discharge profile of M-LR-NCM with different conditions at 25 mA g^{-1} between 2.0 to 4.8 V.

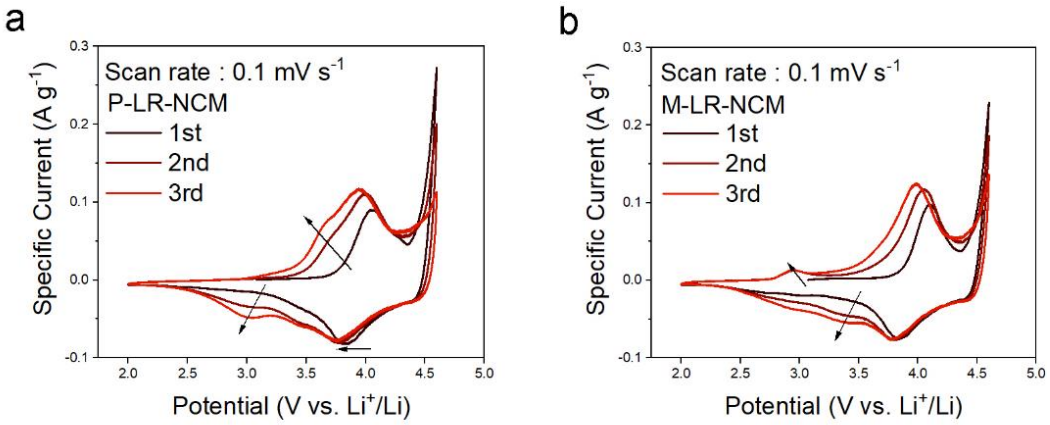

Figure S14. CVs for the initial three cycles of (a) P-LR-NCM and (b) M-LR-NCM at 0.1 mV s^{-1} scan rate.

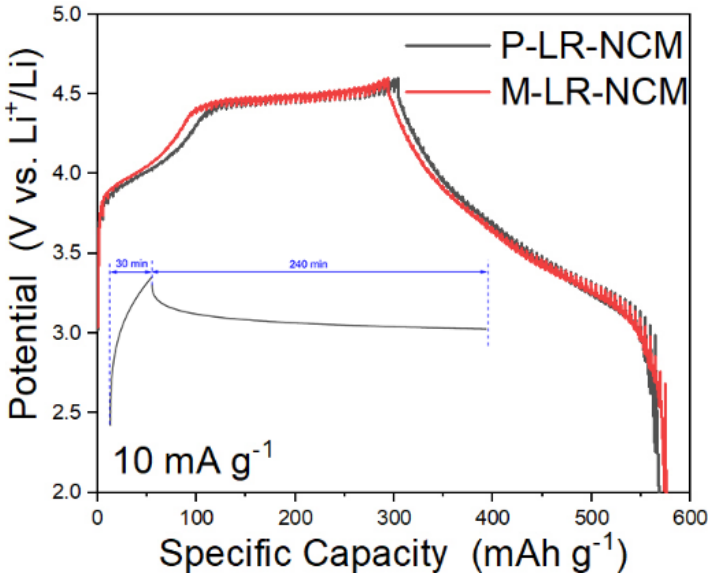

Figure S15. GITT results of P-LR-NCM and M-LR-NCM during first cycle. The inset is a schematic illustration of a single step of the GITT with the interval 30 min charge or discharge at a specific current of 10 mA g^{-1} and 240 min relaxation.

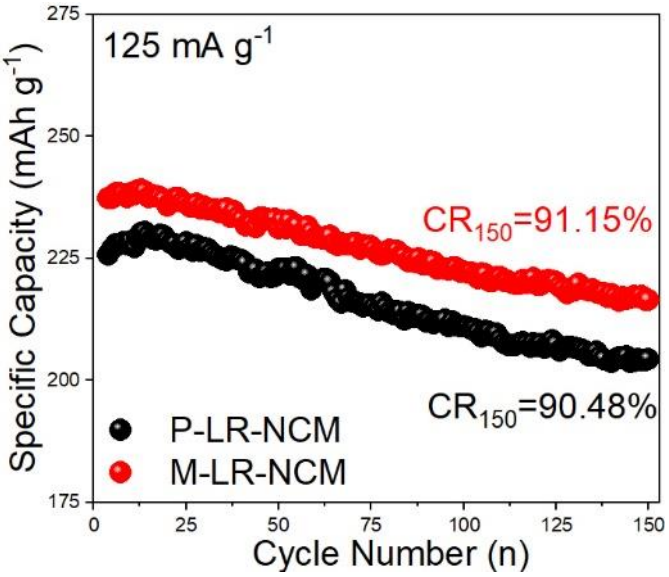

Figure S16. The cycling performance of P-LR-NCM and M-LR-NCM at 125 mA g^{-1}.

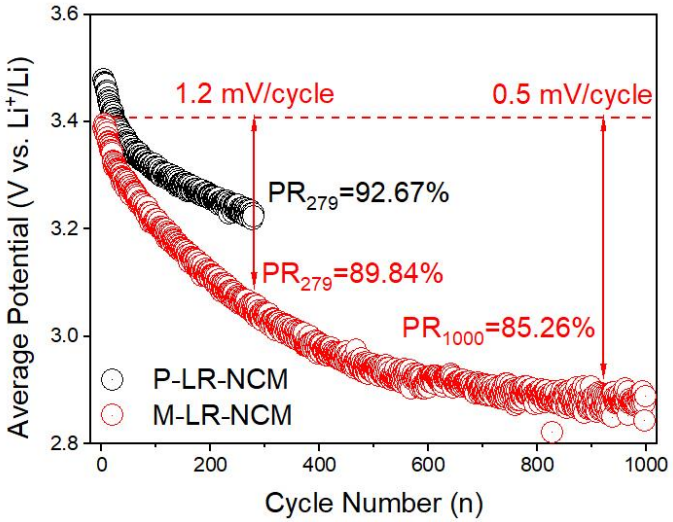

Figure S17. The potential decay of P-LR-NCM and M-LR-NCM at 250 mA g^{-1}.

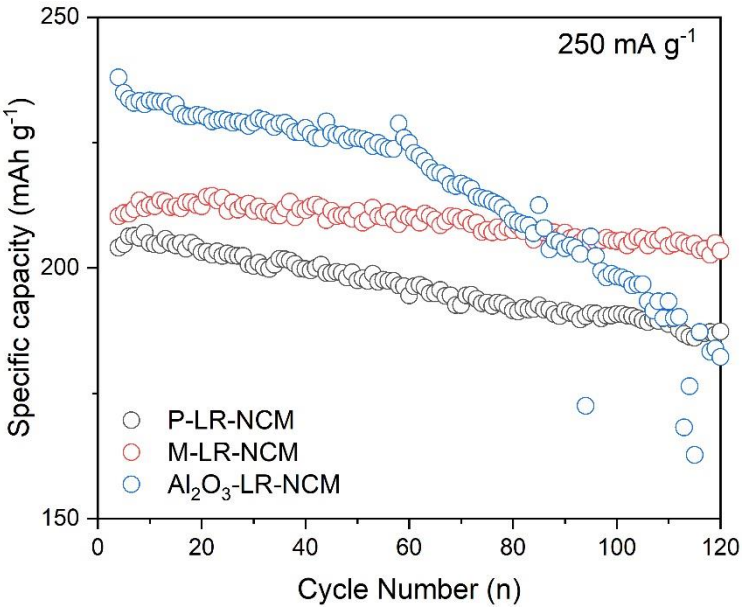

Figure S18. The specific discharging capacity of P-LR-NCM, M-LR-NCM and Al_2O_3-LR-NCM (Al_2O_3 coated P-LR-NCM) at 250 mA g^{-1} during 120 cycles.

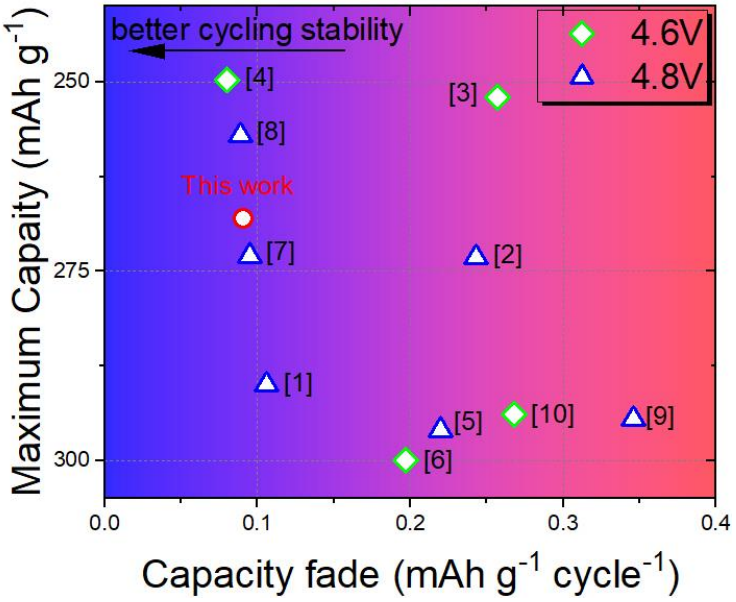

Figure S19. Electrochemical performance comparisons with other mainstream reports.

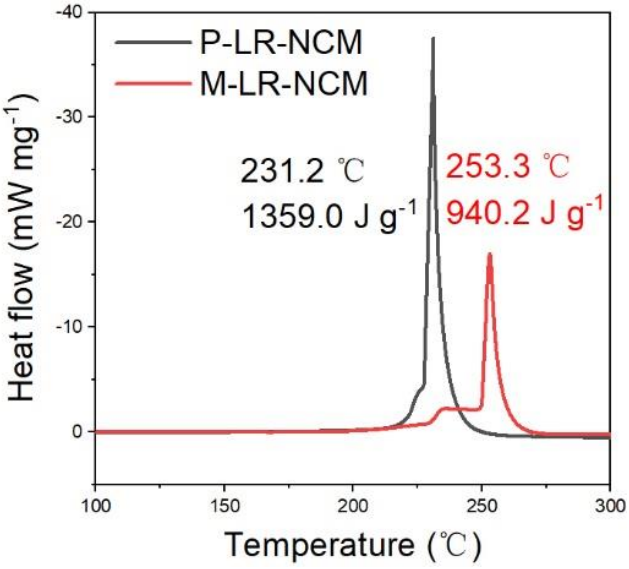

Figure S20. DSC results of P-LR-NCM and M-LR-NCM after charging to 4.8V.

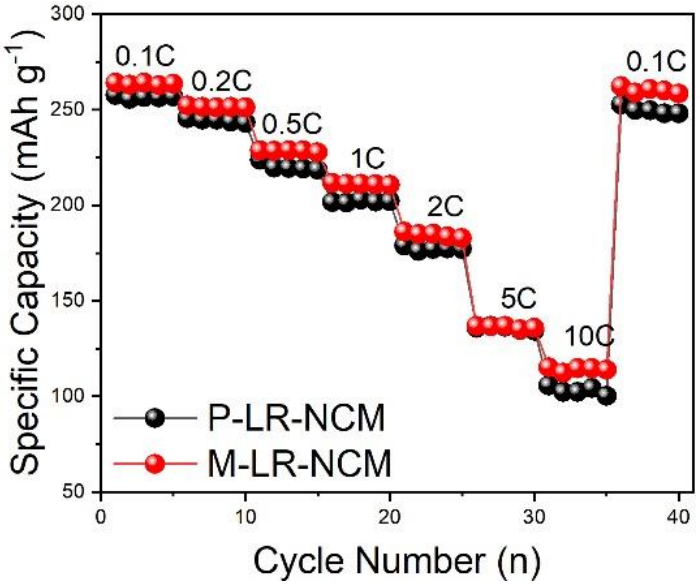

Figure S21. The rate performance of P-LR-NCM and M-LR-NCM at room temperature.

Table S3. Summarized electrochemical performances of advanced LR-NCM materials from mainstream reports. The symbol ~ indicates estimated values from figures of each reference.

Modification	Capacity Maximum	Cycling Performances			Test conditions
	@RT (mAh g^{-1})	Specific capacity (mAh g^{-1})	Capacity retention	Average Capacity fade (mAh g^{-1} cycle $^{-1}$)	Specific current (mA g^{-1})
Ref[1]-Spinel $LiCoO_2$[3]	290 (12.5 mA g^{-1} 4.8V)	205	79.3% at 400th	0.106	250
Ref[2]-$LiTaO_3$ ALD coating[4]	273.2 (20 mA g^{-1} 4.8V)	~220	78% at 200th	0.243	200
Ref[3]-Ammonia treatment @400 ^oC[5]	252 (25 mA g^{-1})	226	93.3% at 60th	0.257	83.3
Ref[4]-H_2SO_4 treatment[6]	249.7 (25 mA g^{-1})	196.5	79.8% at 500th	0.080	250
Ref[5]-oleic acid[7]	296 (25 mA g^{-1} 4.8V)	277	84.1% at 200th	0.220	250
Ref[6]-$NH_3 \cdot H_20$[8]	300 (20 mA g^{-1})	~261	85% at 200th	0.197	100
Ref[7]-$NiFe_2O_4$[9]	273 (26mA g^{-1} 4.8V)	232.5	91.8% at 200th	0.095	260
Ref[8]- Ni-rich surface[10]	257.1 (25 mA g^{-1} 4.8V)	232	92.3% at 200th	0.089	250
Ref[9]-Yb doping[11]	294.5 (26 mA g^{-1} 4.8V)	219.8	84.4% at 100th	0.346	250
Ref[10]-B doping[12]	293.9 (10 mA g^{-1})	255.4	89.5% at 100th	0.268	100
This work	268.1 (25 mA g^{-1})	210.3	57.0% at 1000th	0.091	250

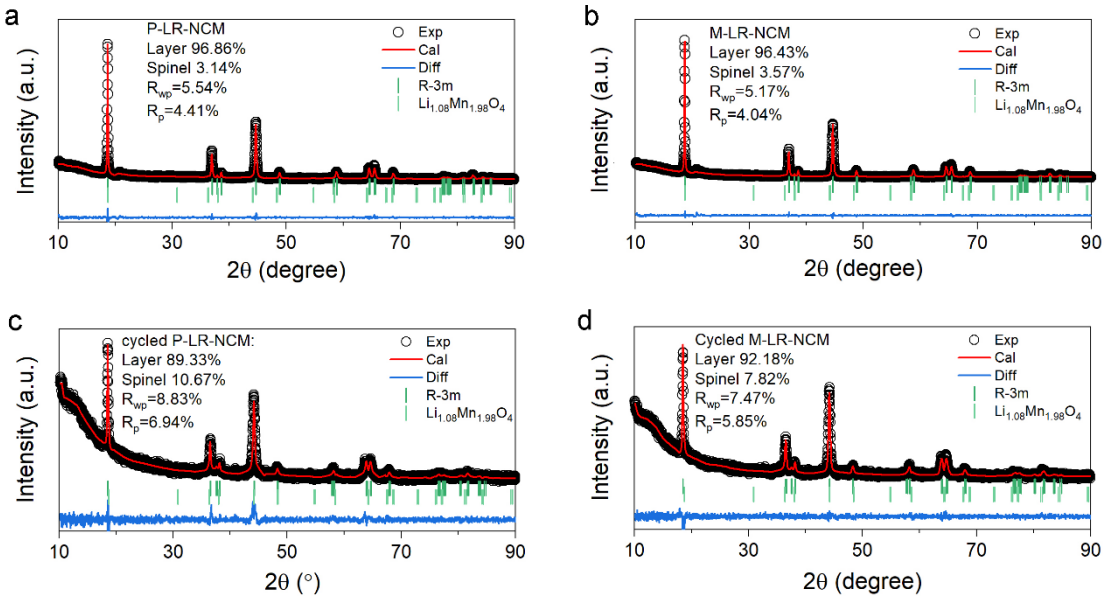

Figure S22. Rietveld refinement XRD through FullProf via double phase models. (R-3m and Fd-3m). (a)P-LR-NCM, (b) M-LR-NCM, (c) cycled P-LR-NCM and (d) cycled M-LR-NCM.

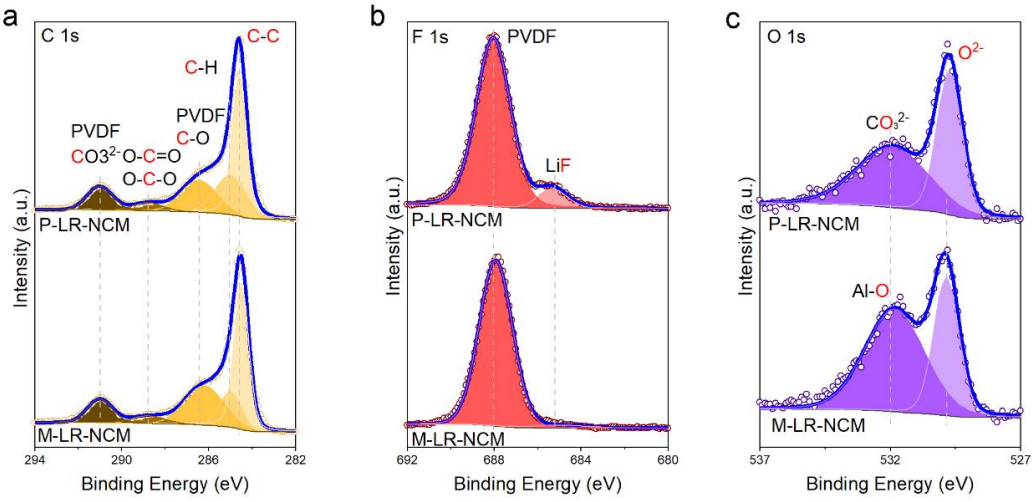

Figure S23. Comparison of XPS spectra of (a) C 1s, (b) F 1s and (c) O 1s of P-LR-NCM and M-LR-NCM before cycling.

Table S4. Results of the Rietveld analysis for P-LR-NCM and M-LR-NCM after 200 cycle at 1C from FullProf. And related micro-strain analysis from JADE.

Sample	*a*/Å	*c*/Å	Li/Ni Mixing	R_{wp}/%	R_p/%	Strain(%)
P-LR-NCM	2.8890	14.424	0.006	5.50	6.98	0.471(0.0108)
M-LR-NCM	2.8810	14.370	0.005	5.48	6.97	0.362(0.0097)

References

1. R. A. House, J.-J. Marie, M. A. Pérez-Osorio, G. J. Rees, E. Boivin and P. G. Bruce, *Nat. Energy*, 2021, **6**, 781-789.
2. X. D. Zhang, J. L. Shi, J. Y. Liang, Y. X. Yin, J. N. Zhang, X. Q. Yu and Y. G. Guo, *Adv. Mater.*, 2018, **30**, 1801751.
3. Y. Liu, H. Zhu, H. Zhu, Y. Ren, Y. Zhu, Y. Huang, L. Dai, S. Dou, J. Xu, C. J. Sun, X. L. Wang, Y. Deng, Q. Yuan, X. Liu, J. Wu, Y. Chen and Q. Liu, *Adv. Energy Mater.*, 2021, **11**, 2003479.
4. E. Wang, Y. Zhao, D. Xiao, X. Zhang, T. Wu, B. Wang, M. Zubair, Y. Li, X. Sun and H. Yu, *Adv. Mater.*, 2020, **32**, 1906070.
5. E. M. Erickson, H. Sclar, F. Schipper, J. Liu, R. Tian, C. Ghanty, L. Burstein, N. Leifer, J. Grinblat, M. Talianker, J.-Y. Shin, J. K. Lampert, B. Markovsky, A. I. Frenkel and D. Aurbach, *Adv. Energy Mater.*, 2017, **7**, 1700708.
6. H. C. Guo, Z. Wei, K. Jia, B. Qiu, C. Yin, F. Q. Meng, Q. H. Zhang, L. Gu, S. J. Han, Y. Liu, H. Zhao, W. Jiang, H. F. Cui, Y. G. Xia and Z. P. Liu, *Energy Storage Mater.*, 2019, **16**, 220-227.
7. W. Guo, C. Zhang, Y. Zhang, L. Lin, W. He, Q. Xie, B. Sa, L. Wang and D. L. Peng, *Adv. Mater.*, 2021, **33**, 2103173.
8. B. Wu, X. Yang, X. Jiang, Y. Zhang, H. Shu, P. Gao, L. Liu and X. Wang, *Adv. Funct. Mater.*, 2018, **28**, 1803392.
9. J. Peng, Y. Li, Z. Chen, G. Liang, S. Hu, T. Zhou, F. Zheng, Q. Pan, H. Wang, Q. Li, J. Liu and Z. Guo, *ACS Nano*, 2021, 15, 11607-11618.
10. H. Zheng, Z. Hu, P. Liu, W. Xu, Q. Xie, W. He, Q. Luo, L. Wang, D. Gu, B. Qu, Z.-Z. Zhu and D.-L. Peng, *Energy Storage Mater.*, 2020, **25**, 76-85.
11. L. Bao, Z. Yang, L. Chen, Y. Su, Y. Lu, W. Li, F. Yuan, J. Dong, Y. Fang, Z. Ji, C. Shi and W. Feng, *ChemSusChem*, 2019, **12**, 2294-2301.
12. Z. H. Sun, L. Q. Xu, C. Q. Dong, H. T. Zhang, M. T. Zhang, Y. Y. Liu, Y. Zhou, Y. Han and Y. S. Chen, *J. Mater. Chem. A*, 2019, **7**, 3375-3383.